Observation of an Altered $a_0(980)$ Line shape in $D^+ \to \pi^+\eta\eta$

M. Ablikim[1], M. N. Achasov[4,b], P. Adlarson[77], X. C. Ai[82], R. Aliberti[36], A. Amoroso[76A,76C], Q. An[73,59,†], Y. Bai[58], O. Bakina[37], Y. Ban[47,g], H.-R. Bao[65], V. Batozskaya[1,45], K. Begzsuren[33], N. Berger[36], M. Berlowski[45], M. Bertani[29A], D. Bettoni[30A], F. Bianchi[76A,76C], E. Bianco[76A,76C], A. Bortone[76A,76C], I. Boyko[37], R. A. Briere[5], A. Brueggemann[70], H. Cai[78], M. H. Cai[39,j,k], X. Cai[1,59], A. Calcaterra[29A], G. F. Cao[1,65], N. Cao[1,65], S. A. Cetin[63A], X. Y. Chai[47,g], J. F. Chang[1,59], G. R. Che[44], Y. Z. Che[1,59,65], C. H. Chen[9], Chao Chen[56], G. Chen[1], H. S. Chen[1,65], H. Y. Chen[21], M. L. Chen[1,59,65], S. J. Chen[43], S. L. Chen[46], S. M. Chen[62], T. Chen[1,65], X. R. Chen[32,65], X. T. Chen[1,65], X. Y. Chen[12,f], Y. B. Chen[1,59], Y. Q. Chen[35], Y. Q. Chen[16], Z. J. Chen[26,h], Z. K. Chen[60], S. K. Choi[10], X. Chu[12,f], G. Cibinetto[30A], F. Cossio[76C], J. Cottee-Meldrum[64], J. J. Cui[51], H. L. Dai[1,59], J. P. Dai[80], A. Dbeyssi[19], R. E. de Boer[3], D. Dedovich[37], C. Q. Deng[74], Z. Y. Deng[1], A. Denig[36], I. Denysenko[37], M. Destefanis[76A,76C], F. De Mori[76A,76C], B. Ding[68,1], X. X. Ding[47,g], Y. Ding[41], Y. Ding[35], Y. X. Ding[31], J. Dong[1,59], L. Y. Dong[1,65], M. Y. Dong[1,59,65], X. Dong[78], M. C. Du[1], S. X. Du[82], S. X. Du[12,f], Y. Y. Duan[56], P. Egorov[37,a], G. F. Fan[43], J. J. Fan[20], Y. H. Fan[46], J. Fang[1,59], J. Fang[60], S. S. Fang[1,65], W. X. Fang[1], Y. Q. Fang[1,59], R. Farinelli[30A], L. Fava[76B,76C], F. Feldbauer[3], G. Felici[29A], C. Q. Feng[73,59], J. H. Feng[16], L. Feng[39,j,k], Q. X. Feng[39,j,k], Y. T. Feng[73,59], M. Fritsch[3], C. D. Fu[1], J. L. Fu[65], Y. W. Fu[1,65], H. Gao[65], X. B. Gao[42], Y. Gao[73,59], Y. N. Gao[47,g], Y. N. Gao[20], Y. Y. Gao[31], S. Garbolino[76C], I. Garzia[30A,30B], P. T. Ge[20], Z. W. Ge[43], C. Geng[60], E. M. Gersabeck[69], A. Gilman[71], K. Goetzen[13], J. D. Gong[35], L. Gong[41], W. X. Gong[1,59], W. Gradl[36], S. Gramigna[30A,30B], M. Greco[76A,76C], M. H. Gu[1,59], Y. T. Gu[15], C. Y. Guan[1,65], A. Q. Guo[32], L. B. Guo[42], M. J. Guo[51], R. P. Guo[50], Y. P. Guo[12,f], A. Guskov[37,a], J. Gutierrez[28], K. L. Han[65], T. T. Han[1], F. Hanisch[3], K. D. Hao[73,59], X. Q. Hao[20], F. A. Harris[67], K. K. He[56], K. L. He[1,65], F. H. Heinsius[3], C. H. Heinz[36], Y. K. Heng[1,59,65], C. Herold[61], P. C. Hong[35], G. Y. Hou[1,65], X. T. Hou[1,65], Y. R. Hou[65], Z. L. Hou[1], H. M. Hu[1,65], J. F. Hu[57,i], Q. P. Hu[73,59], S. L. Hu[12,f], T. Hu[1,59,65], Y. Hu[1], Z. M. Hu[60], G. S. Huang[73,59], K. X. Huang[60], L. Q. Huang[32,65], P. Huang[43], X. T. Huang[51], Y. P. Huang[1], Y. S. Huang[60], T. Hussain[75], N. Hüsken[36], N. in der Wiesche[70], J. Jackson[28], Q. Ji[1], Q. P. Ji[20], W. Ji[1,65], X. B. Ji[1,65], X. L. Ji[1,59], Y. Y. Ji[51], Z. K. Jia[73,59], D. Jiang[1,65], H. B. Jiang[78], P. C. Jiang[47,g], S. J. Jiang[9], T. J. Jiang[17], X. S. Jiang[1,59,65], Y. Jiang[65], J. B. Jiao[51], J. K. Jiao[35], Z. Jiao[24], S. Jin[43], Y. Jin[68], M. Q. Jing[1,65], X. M. Jing[65], T. Johansson[77], S. Kabana[34], N. Kalantar-Nayestanaki[66], X. L. Kang[9], X. S. Kang[41], M. Kavatsyuk[66], B. C. Ke[82], V. Khachatryan[28], A. Khoukaz[70], R. Kiuchi[1], O. B. Kolcu[63A], B. Kopf[3], M. Kuessner[3], X. Kui[1,65], N. Kumar[27], A. Kupsc[45,77], W. Kühn[38], Q. Lan[74], W. N. Lan[20], T. T. Lei[73,59], M. Lellmann[36], T. Lenz[36], C. Li[73,59], C. Li[48], C. Li[44], C. H. Li[40], C. K. Li[21], D. M. Li[82], F. Li[1,59], G. Li[1], H. B. Li[1,65], H. J. Li[20], H. N. Li[57,i], Hui Li[44], J. R. Li[62], J. S. Li[60], K. Li[1], K. L. Li[20], K. L. Li[39,j,k], L. J. Li[1,65], Lei Li[49], M. H. Li[44], M. R. Li[1,65], P. L. Li[65], P. R. Li[39,j,k], Q. M. Li[1,65], Q. X. Li[51], R. Li[18,32], S. X. Li[12], T. Li[51], T. Y. Li[44], W. D. Li[1,65], W. G. Li[1,†], X. Li[1,65], X. H. Li[73,59], X. L. Li[51], X. Y. Li[1,8], X. Z. Li[60], Y. Li[20], Y. G. Li[47,g], Y. P. Li[35], Z. J. Li[60], Z. Y. Li[80], H. Liang[73,59], Y. F. Liang[55], Y. T. Liang[32,65], G. R. Liao[14], L. B. Liao[60], M. H. Liao[60], Y. P. Liao[1,65], J. Libby[27], A. Limphirat[61], C. C. Lin[56], D. X. Lin[32,65], L. Q. Lin[40], T. Lin[1], B. J. Liu[1], B. X. Liu[78], C. Liu[35], C. X. Liu[1], F. Liu[1], F. H. Liu[54], Feng Liu[6], G. M. Liu[57,i], H. Liu[39,j,k], H. B. Liu[15], H. H. Liu[1], H. M. Liu[1,65], Huihui Liu[22], J. B. Liu[73,59], J. J. Liu[21], K. Liu[39,j,k], K. Liu[74], K. Y. Liu[41], Ke Liu[23], L. Liu[73,59], L. C. Liu[44], Lu Liu[44], M. H. Liu[12,f], P. L. Liu[1], Q. Liu[65], S. B. Liu[73,59], T. Liu[12,f], W. K. Liu[44], W. M. Liu[73,59], W. T. Liu[40], X. Liu[39,j,k], X. Liu[40], X. K. Liu[39,j,k], X. Y. Liu[78], Y. Liu[39,j,k], Y. Liu[82], Yuan Liu[82], Y. B. Liu[44], Z. A. Liu[1,59,65], Z. D. Liu[9], Z. Q. Liu[51], X. C. Lou[1,59,65], F. X. Lu[60], H. J. Lu[24], J. G. Lu[1,59], X. L. Lu[16], Y. Lu[7], Y. H. Lu[1,65], Y. P. Lu[1,59], Z. H. Lu[1,65], C. L. Luo[42], J. R. Luo[60], J. S. Luo[1,65], M. X. Luo[81], T. Luo[12,f], X. L. Luo[1,59], Z. Y. Lv[23], X. R. Lyu[65,o], Y. F. Lyu[44], Y. H. Lyu[82], F. C. Ma[41], H. L. Ma[1], J. L. Ma[1,65], L. L. Ma[51], L. R. Ma[68], Q. M. Ma[1], R. Q. Ma[1,65], R. Y. Ma[20], T. Ma[73,59], X. T. Ma[1,65], X. Y. Ma[1,59], Y. M. Ma[32], F. E. Maas[19], I. MacKay[71], M. Maggiora[76A,76C], S. Malde[71], Q. A. Malik[75], H. X. Mao[39,j,k], Y. J. Mao[47,g], Z. P. Mao[1], S. Marcello[76A,76C], A. Marshall[64], F. M. Melendi[30A,30B], Y. H. Meng[65], Z. X. Meng[68], G. Mezzadri[30A], H. Miao[1,65], T. J. Min[43], R. E. Mitchell[28], X. H. Mo[1,59,65], B. Moses[28], N. Yu. Muchnoi[4,b], J. Muskalla[36], Y. Nefedov[37], F. Nerling[19,d], L. S. Nie[21], I. B. Nikolaev[4,b], Z. Ning[1,59], S. Nisar[11,l], Q. L. Niu[39,j,k], W. D. Niu[12,f], C. Normand[64], S. L. Olsen[10,65], Q. Ouyang[1,59,65], S. Pacetti[29B,29C], X. Pan[56], Y. Pan[58], A. Pathak[10], Y. P. Pei[73,59], M. Pelizaeus[3], H. P. Peng[73,59], X. J. Peng[39,j,k], Y. Y. Peng[39,j,k], K. Peters[13,d], K. Petridis[64], J. L. Ping[42], R. G. Ping[1,65], S. Plura[36], V. Prasad[34], F. Z. Qi[1], H. R. Qi[62], M. Qi[43], S. Qian[1,59], W. B. Qian[65], C. F. Qiao[65], J. H. Qiao[20], J. J. Qin[74], J. L. Qin[56], L. Q. Qin[14], L. Y. Qin[73,59], P. B. Qin[74], X. P. Qin[12,f], X. S. Qin[51], Z. H. Qin[1,59], J. F. Qiu[1], Z. H. Qu[74], J. Rademacker[64], C. F. Redmer[36], A. Rivetti[76C], M. Rolo[76C], G. Rong[1,65], S. S. Rong[1,65], F. Rosini[29B,29C], Ch. Rosner[19], M. Q. Ruan[1,59], N. Salone[45], A. Sarantsev[37,c], Y. Schelhaas[36], K. Schoenning[77], M. Scodeggio[30A], K. Y. Shan[12,f], W. Shan[25], X. Y. Shan[73,59], Z. J. Shang[39,j,k], J. F. Shangguan[17], L. G. Shao[1,65], M. Shao[73,59], C. P. Shen[12,f], H. F. Shen[1,8], W. H. Shen[65], X. Y. Shen[1,65], B. A. Shi[65], H. Shi[73,59], J. L. Shi[12,f], J. Y. Shi[1], S. Y. Shi[74], X. Shi[1,59], H. L. Song[73,59], J. J. Song[20], T. Z. Song[60], W. M. Song[35], Y. J. Song[12,f], Y. X. Song[47,g,m], S. Sosio[76A,76C], S. Spataro[76A,76C], F. Stieler[36], S. S Su[41], Y. J. Su[65],

G. B. Sun[78], G. X. Sun[1], H. Sun[65], H. K. Sun[1], J. F. Sun[20], K. Sun[62], L. Sun[78], S. S. Sun[1,65], T. Sun[52,e], Y. C. Sun[78], Y. H. Sun[31], Y. J. Sun[73,59], Y. Z. Sun[1], Z. Q. Sun[1,65], Z. T. Sun[51], C. J. Tang[55], G. Y. Tang[1], J. Tang[60], J. J. Tang[73,59], L. F. Tang[40], Y. A. Tang[78], L. Y. Tao[74], M. Tat[71], J. X. Teng[73,59], J. Y. Tian[73,59], W. H. Tian[60], Y. Tian[32], Z. F. Tian[78], I. Uman[63B], B. Wang[1], B. Wang[60], Bo Wang[73,59], C. Wang[39,j,k], C. Wang[20], Cong Wang[23], D. Y. Wang[47,g], H. J. Wang[39,j,k], J. J. Wang[78], K. Wang[1,59], L. L. Wang[1], L. W. Wang[35], M. Wang[51], M. Wang[73,59], N. Y. Wang[65], S. Wang[12,f], T. Wang[12,f], T. J. Wang[44], W. Wang[60], Wei Wang[74], W. P. Wang[36,73,59,n], X. Wang[47,g], X. F. Wang[39,j,k], X. J. Wang[40], X. L. Wang[12,f], X. N. Wang[1], Y. Wang[62], Y. D. Wang[46], Y. F. Wang[1,59,65], Y. H. Wang[39,j,k], Y. J. Wang[73,59], Y. L. Wang[20], Y. N. Wang[78], Y. Q. Wang[1], Yaqian Wang[18], Yi Wang[62], Yuan Wang[18,32], Z. Wang[1,59], Z. L. Wang[74], Z. L. Wang[2], Z. Q. Wang[12,f], Z. Y. Wang[1,65], D. H. Wei[14], H. R. Wei[44], F. Weidner[70], S. P. Wen[1], Y. R. Wen[40], U. Wiedner[3], G. Wilkinson[71], M. Wolke[77], C. Wu[40], J. F. Wu[1,8], L. H. Wu[1], L. J. Wu[1,65], L. J. Wu[20], Lianjie Wu[20], S. G. Wu[1,65], S. M. Wu[65], X. Wu[12,f], X. H. Wu[35], Y. J. Wu[32], Z. Wu[1,59], L. Xia[73,59], X. M. Xian[40], B. H. Xiang[1,65], D. Xiao[39,j,k], G. Y. Xiao[43], H. Xiao[74], Y. L. Xiao[12,f], Z. J. Xiao[42], C. Xie[43], K. J. Xie[1,65], X. H. Xie[47,g], Y. Xie[51], Y. G. Xie[1,59], Y. H. Xie[6], Z. P. Xie[73,59], T. Y. Xing[1,65], C. F. Xu[1,65], C. J. Xu[60], G. F. Xu[1], H. Y. Xu[68,2], H. Y. Xu[2], M. Xu[73,59], Q. J. Xu[17], Q. N. Xu[31], T. D. Xu[74], W. Xu[1], W. L. Xu[68], X. P. Xu[56], Y. Xu[41], Y. Xu[12,f], Y. C. Xu[79], Z. S. Xu[65], F. Yan[12,f], H. Y. Yan[40], L. Yan[12,f], W. B. Yan[73,59], W. C. Yan[82], W. H. Yan[6], W. P. Yan[20], X. Q. Yan[1,65], H. J. Yang[52,e], H. L. Yang[35], H. X. Yang[1], J. H. Yang[43], R. J. Yang[20], T. Yang[1], Y. Yang[12,f], Y. F. Yang[44], Y. H. Yang[43], Y. Q. Yang[9], Y. X. Yang[1,65], Y. Z. Yang[20], M. Ye[1,59], M. H. Ye[8], Z. J. Ye[57,i], Junhao Yin[44], Z. Y. You[60], B. X. Yu[1,59,65], C. X. Yu[44], G. Yu[13], J. S. Yu[26,h], L. Q. Yu[12,f], M. C. Yu[41], T. Yu[74], X. D. Yu[47,g], Y. C. Yu[82], C. Z. Yuan[1,65], H. Yuan[1,65], J. Yuan[35], J. Yuan[46], L. Yuan[2], S. C. Yuan[1,65], X. Q. Yuan[1], Y. Yuan[1,65], Z. Y. Yuan[60], C. X. Yue[40], Ying Yue[20], A. A. Zafar[75], S. H. Zeng[64], X. Zeng[12,f], Y. Zeng[26,h], Yujie Zeng[60], Y. J. Zeng[1,65], X. Y. Zhai[35], Y. H. Zhan[60], A. Q. Zhang[1,65], B. L. Zhang[1,65], B. X. Zhang[1], D. H. Zhang[44], G. Y. Zhang[20], G. Y. Zhang[1,65], H. Zhang[73,59], H. Zhang[82], H. C. Zhang[1,59,65], H. H. Zhang[60], H. Q. Zhang[1,59,65], H. R. Zhang[73,59], H. Y. Zhang[1,59], Jin Zhang[82], J. Zhang[60], J. J. Zhang[53], J. L. Zhang[21], J. Q. Zhang[42], J. S. Zhang[12,f], J. W. Zhang[1,59,65], J. X. Zhang[39,j,k], J. Y. Zhang[1], J. Z. Zhang[1,65], Jianyu Zhang[65], L. M. Zhang[62], Lei Zhang[43], N. Zhang[82], P. Zhang[1,8], Q. Zhang[20], Q. Y. Zhang[35], R. Y. Zhang[39,j,k], S. H. Zhang[1,65], Shulei Zhang[26,h], X. M. Zhang[1], X. Y Zhang[41], X. Y. Zhang[51], Y. Zhang[1], Y. Zhang[74], Y. T. Zhang[82], Y. H. Zhang[1,59], Y. M. Zhang[40], Y. P. Zhang[73,59], Z. D. Zhang[1], Z. H. Zhang[1], Z. L. Zhang[35], Z. L. Zhang[56], Z. X. Zhang[20], Z. Y. Zhang[78], Z. Y. Zhang[44], Z. Z. Zhang[46], Zh. Zh. Zhang[20], G. Zhao[1], J. Y. Zhao[1,65], J. Z. Zhao[1,59], L. Zhao[1], L. Zhao[73,59], M. G. Zhao[44], N. Zhao[80], R. P. Zhao[65], S. J. Zhao[82], Y. B. Zhao[1,59], Y. L. Zhao[56], Y. X. Zhao[32,65], Z. G. Zhao[73,59], A. Zhemchugov[37,a], B. Zheng[74], B. M. Zheng[35], J. P. Zheng[1,59], W. J. Zheng[1,65], X. R. Zheng[20], Y. H. Zheng[65,o], B. Zhong[42], C. Zhong[20], H. Zhou[36,51,n], J. Q. Zhou[35], J. Y. Zhou[35], S. Zhou[6], X. Zhou[78], X. K. Zhou[6], X. R. Zhou[73,59], X. Y. Zhou[40], Y. X. Zhou[79], Y. Z. Zhou[12,f], A. N. Zhu[65], J. Zhu[44], K. Zhu[1], K. J. Zhu[1,59,65], K. S. Zhu[12,f], L. Zhu[35], L. X. Zhu[65], S. H. Zhu[72], T. J. Zhu[12,f], W. D. Zhu[42], W. D. Zhu[12,f], W. J. Zhu[1], W. Z. Zhu[20], Y. C. Zhu[73,59], Z. A. Zhu[1,65], X. Y. Zhuang[44], J. H. Zou[1], J. Zu[73,59]

(BESIII Collaboration)

[1] *Institute of High Energy Physics, Beijing 100049, People's Republic of China*
[2] *Beihang University, Beijing 100191, People's Republic of China*
[3] *Bochum Ruhr-University, D-44780 Bochum, Germany*
[4] *Budker Institute of Nuclear Physics SB RAS (BINP), Novosibirsk 630090, Russia*
[5] *Carnegie Mellon University, Pittsburgh, Pennsylvania 15213, USA*
[6] *Central China Normal University, Wuhan 430079, People's Republic of China*
[7] *Central South University, Changsha 410083, People's Republic of China*
[8] *China Center of Advanced Science and Technology, Beijing 100190, People's Republic of China*
[9] *China University of Geosciences, Wuhan 430074, People's Republic of China*
[10] *Chung-Ang University, Seoul, 06974, Republic of Korea*
[11] *COMSATS University Islamabad, Lahore Campus, Defence Road, Off Raiwind Road, 54000 Lahore, Pakistan*
[12] *Fudan University, Shanghai 200433, People's Republic of China*
[13] *GSI Helmholtzcentre for Heavy Ion Research GmbH, D-64291 Darmstadt, Germany*
[14] *Guangxi Normal University, Guilin 541004, People's Republic of China*
[15] *Guangxi University, Nanning 530004, People's Republic of China*
[16] *Guangxi University of Science and Technology, Liuzhou 545006, People's Republic of China*
[17] *Hangzhou Normal University, Hangzhou 310036, People's Republic of China*
[18] *Hebei University, Baoding 071002, People's Republic of China*
[19] *Helmholtz Institute Mainz, Staudinger Weg 18, D-55099 Mainz, Germany*
[20] *Henan Normal University, Xinxiang 453007, People's Republic of China*
[21] *Henan University, Kaifeng 475004, People's Republic of China*
[22] *Henan University of Science and Technology, Luoyang 471003, People's Republic of China*
[23] *Henan University of Technology, Zhengzhou 450001, People's Republic of China*

[24] *Huangshan College, Huangshan 245000, People's Republic of China*
[25] *Hunan Normal University, Changsha 410081, People's Republic of China*
[26] *Hunan University, Changsha 410082, People's Republic of China*
[27] *Indian Institute of Technology Madras, Chennai 600036, India*
[28] *Indiana University, Bloomington, Indiana 47405, USA*
[29] *INFN Laboratori Nazionali di Frascati, (A)INFN Laboratori Nazionali di Frascati, I-00044, Frascati, Italy; (B)INFN Sezione di Perugia, I-06100, Perugia, Italy; (C)University of Perugia, I-06100, Perugia, Italy*
[30] *INFN Sezione di Ferrara, (A)INFN Sezione di Ferrara, I-44122, Ferrara, Italy; (B)University of Ferrara, I-44122, Ferrara, Italy*
[31] *Inner Mongolia University, Hohhot 010021, People's Republic of China*
[32] *Institute of Modern Physics, Lanzhou 730000, People's Republic of China*
[33] *Institute of Physics and Technology, Mongolian Academy of Sciences, Peace Avenue 54B, Ulaanbaatar 13330, Mongolia*
[34] *Instituto de Alta Investigación, Universidad de Tarapacá, Casilla 7D, Arica 1000000, Chile*
[35] *Jilin University, Changchun 130012, People's Republic of China*
[36] *Johannes Gutenberg University of Mainz, Johann-Joachim-Becher-Weg 45, D-55099 Mainz, Germany*
[37] *Joint Institute for Nuclear Research, 141980 Dubna, Moscow region, Russia*
[38] *Justus-Liebig-Universitaet Giessen, II. Physikalisches Institut, Heinrich-Buff-Ring 16, D-35392 Giessen, Germany*
[39] *Lanzhou University, Lanzhou 730000, People's Republic of China*
[40] *Liaoning Normal University, Dalian 116029, People's Republic of China*
[41] *Liaoning University, Shenyang 110036, People's Republic of China*
[42] *Nanjing Normal University, Nanjing 210023, People's Republic of China*
[43] *Nanjing University, Nanjing 210093, People's Republic of China*
[44] *Nankai University, Tianjin 300071, People's Republic of China*
[45] *National Centre for Nuclear Research, Warsaw 02-093, Poland*
[46] *North China Electric Power University, Beijing 102206, People's Republic of China*
[47] *Peking University, Beijing 100871, People's Republic of China*
[48] *Qufu Normal University, Qufu 273165, People's Republic of China*
[49] *Renmin University of China, Beijing 100872, People's Republic of China*
[50] *Shandong Normal University, Jinan 250014, People's Republic of China*
[51] *Shandong University, Jinan 250100, People's Republic of China*
[52] *Shanghai Jiao Tong University, Shanghai 200240, People's Republic of China*
[53] *Shanxi Normal University, Linfen 041004, People's Republic of China*
[54] *Shanxi University, Taiyuan 030006, People's Republic of China*
[55] *Sichuan University, Chengdu 610064, People's Republic of China*
[56] *Soochow University, Suzhou 215006, People's Republic of China*
[57] *South China Normal University, Guangzhou 510006, People's Republic of China*
[58] *Southeast University, Nanjing 211100, People's Republic of China*
[59] *State Key Laboratory of Particle Detection and Electronics, Beijing 100049, Hefei 230026, People's Republic of China*
[60] *Sun Yat-Sen University, Guangzhou 510275, People's Republic of China*
[61] *Suranaree University of Technology, University Avenue 111, Nakhon Ratchasima 30000, Thailand*
[62] *Tsinghua University, Beijing 100084, People's Republic of China*
[63] *Turkish Accelerator Center Particle Factory Group, (A)Istinye University, 34010, Istanbul, Turkey; (B)Near East University, Nicosia, North Cyprus, 99138, Mersin 10, Turkey*
[64] *University of Bristol, H H Wills Physics Laboratory, Tyndall Avenue, Bristol, BS8 1TL, UK*
[65] *University of Chinese Academy of Sciences, Beijing 100049, People's Republic of China*
[66] *University of Groningen, NL-9747 AA Groningen, The Netherlands*
[67] *University of Hawaii, Honolulu, Hawaii 96822, USA*
[68] *University of Jinan, Jinan 250022, People's Republic of China*
[69] *University of Manchester, Oxford Road, Manchester, M13 9PL, United Kingdom*
[70] *University of Muenster, Wilhelm-Klemm-Strasse 9, 48149 Muenster, Germany*
[71] *University of Oxford, Keble Road, Oxford OX13RH, United Kingdom*
[72] *University of Science and Technology Liaoning, Anshan 114051, People's Republic of China*
[73] *University of Science and Technology of China, Hefei 230026, People's Republic of China*
[74] *University of South China, Hengyang 421001, People's Republic of China*
[75] *University of the Punjab, Lahore-54590, Pakistan*
[76] *University of Turin and INFN, (A)University of Turin, I-10125, Turin, Italy; (B)University of Eastern Piedmont, I-15121, Alessandria, Italy; (C)INFN, I-10125, Turin, Italy*
[77] *Uppsala University, Box 516, SE-75120 Uppsala, Sweden*
[78] *Wuhan University, Wuhan 430072, People's Republic of China*
[79] *Yantai University, Yantai 264005, People's Republic of China*
[80] *Yunnan University, Kunming 650500, People's Republic of China*
[81] *Zhejiang University, Hangzhou 310027, People's Republic of China*
[82] *Zhengzhou University, Zhengzhou 450001, People's Republic of China*

[†] Deceased
[a] Also at the Moscow Institute of Physics and Technology, Moscow 141700, Russia
[b] Also at the Novosibirsk State University, Novosibirsk, 630090, Russia
[c] Also at the NRC "Kurchatov Institute", PNPI, 188300, Gatchina, Russia
[d] Also at Goethe University Frankfurt, 60323 Frankfurt am Main, Germany
[e] Also at Key Laboratory for Particle Physics, Astrophysics and Cosmology, Ministry of Education; Shanghai Key Laboratory for Particle Physics and Cosmology; Institute of Nuclear and Particle Physics, Shanghai 200240, People's Republic of China
[f] Also at Key Laboratory of Nuclear Physics and Ion-beam Application (MOE) and Institute of Modern Physics, Fudan University, Shanghai 200443, People's Republic of China
[g] Also at State Key Laboratory of Nuclear Physics and Technology, Peking University, Beijing 100871, People's Republic of China
[h] Also at School of Physics and Electronics, Hunan University, Changsha 410082, China
[i] Also at Guangdong Provincial Key Laboratory of Nuclear Science, Institute of Quantum Matter, South China Normal University, Guangzhou 510006, China
[j] Also at MOE Frontiers Science Center for Rare Isotopes, Lanzhou University, Lanzhou 730000, People's Republic of China
[k] Also at Lanzhou Center for Theoretical Physics, Lanzhou University, Lanzhou 730000, People's Republic of China
[l] Also at the Department of Mathematical Sciences, IBA, Karachi 75270, Pakistan
[m] Also at Ecole Polytechnique Federale de Lausanne (EPFL), CH-1015 Lausanne, Switzerland
[n] Also at Helmholtz Institute Mainz, Staudinger Weg 18, D-55099 Mainz, Germany
[o] Also at Hangzhou Institute for Advanced Study, University of Chinese Academy of Sciences, Hangzhou 310024, China

Using 20.3 fb^{-1} of e^+e^- collision data collected with the BESIII detector at $\sqrt{s} = 3.773$ GeV, we perform the first amplitude analysis of the decay $D^+ \to \pi^+\eta\eta$. The intermediate process $D^+ \to a_0(980)^+\eta$, $a_0(980)^+ \to \pi^+\eta$, is observed as the only significant component in the amplitude analysis, and its branching fraction is measured to be $(3.67 \pm 0.12_{\rm stat} \pm 0.06_{\rm syst}) \times 10^{-3}$. The $\pi^+\eta$ mass spectrum associated with $a_0(980)^+\eta$ production exhibits a line shape that differs substantially from those observed in $D_{(s)} \to a_0(980)\pi$ and $D^0 \to a_0(980)^- e^+\nu_e$ decays. We examine several conventional descriptions of the $a_0(980)$ amplitude, including Flatté, dispersively modified Flatté, T-matrix, and K-matrix parameterizations. With reference $a_0(980)$ parameters, neither these models nor their extensions including additional small resonant or non-resonant amplitudes reproduce the observed line shape satisfactorily. When the $a_0(980)$ parameters are allowed to float, satisfactory fits can be obtained, but the pole mass is driven well above the $K\bar{K}$ threshold, inconsistent with the near-threshold character of the $a_0(980)$. The results reveal a tension between fit quality and the physical pole position in conventional direct-production amplitude models.

I. INTRODUCTION

The interpretation of invariant-mass spectra is a central task in hadron spectroscopy. Resonance properties, such as the quantum numbers $I^G J^{PC}$, pole positions, masses, and widths, provide essential information for identifying hadronic states. Among the light hadrons below 1 GeV/c^2, the pseudoscalar and vector mesons are well established, whereas the scalar mesons $f_0(500)$, $K_0^*(700)$, $f_0(980)$, and $a_0(980)$ remain of particular interest because their internal structures are still under discussion. Recent studies of charm-hadron decays involving the $a_0(980)$ have provided important experimental information on its production and line shape [1–5]. In these channels, however, the $a_0(980)$ usually appears together with several other intermediate amplitudes, and the extracted $a_0(980)$ line shape can be affected by interference with them.

The decay $D^+ \to \pi^+\eta\eta$ provides a relatively clean environment for studying the $a_0(980)$ line shape. The upper kinematic boundary of the $\pi^+\eta$ invariant mass, $M(\pi^+\eta)$, is 1.322 GeV/c^2, allowing only a limited set of $\pi^+\eta$ resonant contributions. Besides the $a_0(980)$, the $a_2(1320)$ lies at the kinematic boundary and is strongly suppressed by phase space. Possible contributions in the $\eta\eta$ system are limited to isoscalar states such as $f_0(1370)$, $f_2(1270)$, and $f_0(1500)$ [6]. Considering the available phase space and the known decay branching fractions, these contributions are expected to be small in $D^+ \to \pi^+\eta\eta$. Therefore, this decay is especially suitable for investigating the $D^+ \to a_0(980)^+\eta$ intermediate process and the associated $a_0(980)$ line shape.

In this work, we perform the first amplitude analysis of $D^+ \to \pi^+\eta\eta$ using 20.3 fb^{-1} of e^+e^- collision data collected with the BESIII detector at $\sqrt{s} = 3.773$ GeV [7–9]. We examine a broad set of conventional amplitude models by combining several $a_0(980)$ line shape parameterizations—Flatté [10], dispersively modified Flatté [11], T-matrix [12], and K-matrix [13]—with possible additional cascade decay amplitudes. This study provides a systematic test of how the choice of $a_0(980)$ parameterization affects both the description of the data and the extracted pole position.

II. $a_0(980)$ LINE SHAPE PARAMETERIZATIONS

In this analysis, four descriptions of the $a_0(980)$ line shape are tested: the Flatté parameterization, the dispersively modified Flatté parameterization, the T-matrix formalism, and the K-matrix formalism. These descriptions are introduced below and used in the amplitude fits.

A. Flatté parameterization

Denoting $s \equiv M^2_{\pi\eta}$, the Flatté formula is

$$P_{a_0(980)}(s) = \frac{1}{M_0^2 - s - i\sum_j g_j^2 \rho_j(s)}, \tag{1}$$

where M_0 is the bare mass parameter, g_j is the coupling constant for channel j, and $\rho_j(s)$ is the corresponding phase space factor, defined as

$$\rho_j(s) = \begin{cases} \frac{1}{s}\sqrt{(s-s_j^+)(s-s_j^-)} & s \geq s_j^+ \\ \frac{i}{s}\sqrt{(s_j^+-s)(s-s_j^-)} & s_j^- \leq s < s_j^+ \\ 0 & s < s_j^- \end{cases}, \tag{2}$$

where $s_j^\pm = (m_{j1} \pm m_{j2})^2$, with m_{j1} and m_{j2} being the masses of the two particles in the channel j. The coupled channels considered are $\pi\eta$, $K\bar{K}$, and $\pi\eta'$. Unless otherwise stated, the Flatté parameters are fixed to the values reported by CLEO [14].

B. Dispersively modified Flatté parameterization

The dispersively modified Flatté parameterization is written as

$$P_{a_0(980)}(s) = \frac{1}{M_0^2 - s - \sum_j g_j^2 \Pi_j(s)}, \tag{3}$$

where $\Pi_j(s)$ is the channel-dependent dispersive function defined in Ref. [15]; the same convention and subtraction scheme are used here. Its imaginary part is related to the corresponding two-body phase space, while its real part gives the dispersive threshold correction. Unless otherwise stated, the parameters in this description are fixed to the values reported by BESIII [15].

C. T-matrix formalism

In the T-matrix formalism, we follow the coupled-channel treatment of Ref. [12]. According to the quark-level diagrams considered in that work, the primary tree-level production of $D^+ \to K^+\bar{K}^0\eta$ is absent. The source term is therefore assigned to the $\pi^+\eta$ channel, while the $K^+\bar{K}^0$ channel is generated through coupled-channel final-state interactions. Since the two η mesons in the final state are identical, the total amplitude is symmetrized under $\eta_a \leftrightarrow \eta_b$. Defining $s_a = m^2_{\pi^+\eta_a}$ and $s_b = m^2_{\pi^+\eta_b}$, the amplitude is written as [12]

$$\begin{aligned}\mathcal{M}_{D^+\to\pi^+\eta\eta} = g_1[1 &+ G_{\pi\eta}(s_a)T_{\pi\eta,\pi\eta}(s_a) \\ &+ G_{\pi\eta}(s_b)T_{\pi\eta,\pi\eta}(s_b)],\end{aligned} \tag{4}$$

where g_1 is an overall normalization factor.

The scattering matrix is obtained from the algebraic Bethe-Salpeter equation,

$$T(s) = [1 - V(s)G(s)]^{-1}\, V(s), \tag{5}$$

where V and T are matrices in the coupled-channel space and $G(s) = \mathrm{diag}\,(G_{\pi\eta}(s), G_{K\bar{K}}(s))$. The coupled channels are chosen as (1) $\pi^+\eta$ and (2) $K^+\bar{K}^0$. Following Refs. [12, 16], the potential matrix is

$$\begin{aligned} V_{11} &= -\frac{2m_\pi^2}{3f_{\pi\eta}^2}, \\ V_{12} &= -\frac{3s - m^2_{K^+} - m^2_{\bar{K}^0} - m^2_\eta}{3\sqrt{3}f_{K\bar{K}}f_{\pi\eta}}, \\ V_{22} &= -\frac{s}{4f^2_{K\bar{K}}}, \end{aligned} \tag{6}$$

where the effective decay constants are set to $f_{\pi\eta} = f_{K\bar{K}} = 93$ MeV [16]. For each channel i, the two-point loop function is defined as

$$G_i(s) = i\int \frac{\mathrm{d}^4q}{(2\pi)^4}\frac{1}{(P-q)^2 - m_{i2}^2 + i\epsilon}\frac{1}{q^2 - m_{i1}^2 + i\epsilon}. \tag{7}$$

where $P^2 = s$, and m_{i1} and m_{i2} are the masses of the two particles in the channel i. Following Refs. [12, 16], we use a three-momentum cutoff regularization,

$$G_i(s) = \frac{1}{4\pi^2}\int_0^{q_{\max}} \frac{q^2(\omega_{i1}+\omega_{i2})}{\omega_{i1}\omega_{i2}\left[s - (\omega_{i1}+\omega_{i2})^2 + i\epsilon\right]}\, dq, \tag{8}$$

where $\omega_{ij} = \sqrt{m_{ij}^2 + q^2}$, q is the three-momentum magnitude, and $q_{\max} = 0.6$ GeV is the cutoff.

D. K-matrix formalism

In the S-wave K-matrix formalism, the production amplitude for the channel a is written as

$$F_a(s) = \sum_b \left[I - iK(s)\rho(s)\right]^{-1}_{ab} P_b(s), \tag{9}$$

where I is the identity matrix, $\rho(s)$ is the diagonal matrix of phase space factors, and $P_b(s)$ is the production vector. Following Ref. [13], the coupled channels are chosen as (1) $\pi\eta$, (2) $K\bar{K}$, (3) $\pi\eta'$, and (4) multi-meson states. The corresponding K-matrix is parameterized as

$$K_{ab}(s) = \sum_\alpha \frac{g_a^{(\alpha)} g_b^{(\alpha)}}{M_\alpha^2 - s} + f_{ab}\frac{1.5\ \mathrm{GeV}^2 + s_1}{s + s_1}. \tag{10}$$

The phase space factors for the first three channels are defined using the same convention as in the Flatté parameterization in Eq. 2. For the multi-meson channel, $i = 4$, a smooth threshold form is adopted,

$$\rho_4(s) = \begin{cases} 1 & s \geq s^b_{th} \\ \left(\frac{1 - s^a_{th}/s}{1 - s^a_{th}/s^b_{th}}\right)^{5/2} & s^a_{th} \leq s < s^b_{th} \\ 0 & s < s^a_{th} \end{cases}, \tag{11}$$

where $s^a_{th} = (m_\eta + 3m_\pi)^2$, $s^b_{th} = 2.25\ \mathrm{GeV}^2$.

The production vector describes the coupling of the initial D^+ decay to the coupled channels. We consider the standard form

$$P_a(s) = \sum_\alpha \frac{\beta_\alpha g_a^{(\alpha)}}{M_\alpha^2 - s} + f_a^{\mathrm{prod}}\frac{1.5\ \mathrm{GeV}^2 + s_1^{\mathrm{prod}}}{s + s_1^{\mathrm{prod}}}. \tag{12}$$

The smooth production term is included only in the $\pi\eta$ channel; thus $f_a^{\mathrm{prod}} = 0$ for $a \neq 1$. As an alternative description of the smooth production term, we also consider a polynomial form for the P vector [17],

$$P_a(s) = \sum_\alpha \frac{\beta_\alpha g_a^{(\alpha)}}{M_\alpha^2 - s} + \sum_{n=0}^{1} c_{a,n} s^n, \tag{13}$$

where $c_{a,n} = 0$ for $a \neq 1$.

Following Ref. [13], two bare poles are included in the K-matrix. For the first three channels, the couplings of each bare pole are constrained by

$$g_1^{(\alpha)} = \frac{\cos\Theta}{\sqrt{2}} g^{(\alpha)}, \quad g_2^{(\alpha)} = \frac{\sqrt{\lambda}}{2} g^{(\alpha)}, \quad g_3^{(\alpha)} = \frac{\sin\Theta}{\sqrt{2}} g^{(\alpha)}, \tag{14}$$

where the subscript denotes the channel index, $\Theta \simeq 41.4^\circ$ is the η-η' mixing angle in the quark-flavor basis, and $\lambda = 0.6$ accounts for the suppression of strange-quark-pair creation. The parameters of the K-matrix are listed in Table I.

Finally, for the decay $D^+ \to (\pi^+\eta)_{S-\mathrm{wave}}\eta$, the K-matrix amplitude is symmetrized over the two identical η mesons as

$$A_{D^+\to(\pi^+\eta)_{S-\mathrm{wave}}\eta} = F_1(s_a) + F_1(s_b). \tag{15}$$

TABLE I. K-matrix parameters quoted in Ref.[13]. Masses and couplings are given in GeV/c^2, while units of GeV$^2/c^4$ for s-related quantities are implied, and only f_{11} is non-zero.

	a_0-resonances without K-matrix background term			
	Solution 1		Solution 2	
	$\alpha = 1$	$\alpha = 2$	$\alpha = 1$	$\alpha = 2$
M_α	0.963	1.630	0.965	1.654
$g^{(\alpha)}$	0.879	0.702	0.901	0.435
$g_4^{(\alpha)}$	0.598	0.511	0.689	0.687
	a_0-resonances with K-matrix background term			
	Solution 3		Solution 4	
	$\alpha = 1$	$\alpha = 2$	$\alpha = 1$	$\alpha = 2$
M_α	0.944	1.624	0.939	1.640
$g^{(\alpha)}$	0.879	0.702	0.901	0.435
$g_4^{(\alpha)}$	0.651	0.519	0.653	0.651
	$f_{11} = 0.529$	$s_1 = 1.0$	$f_{11} = 0.731$	$s_1 = 1.9$

E. Discussion

Using the Flatté, dispersively modified Flatté, and T-matrix descriptions introduced above, we compare the corresponding normalized $\pi^+\eta$ mass distributions for the $D^+ \to a_0(980)^+\eta$, $a_0(980)^+ \to \pi^+\eta$ decay chain.

As shown in Fig. 1, the Flatté and dispersively modified Flatté parameterizations give rather similar line shapes, while the T-matrix formalism leads to a visibly different distribution. This difference is expected because, in the implementation used here, the T-matrix amplitude describes the coupled-channel $\pi\eta$ final-state interaction, including both resonant and non-resonant scattering components generated within the model. In contrast, the Flatté and dispersively modified Flatté forms parameterize the $a_0(980)$ propagator with prescribed coupled-channel couplings and do not include an explicit non-resonant $\pi\eta$ scattering background.

The K-matrix result is not shown in this illustrative comparison because its production amplitude depends on the choice of the production vector. In particular, the coefficients β_α describe the relative production strengths of the K-matrix bare poles in the initial D^+ decay, while the smooth production term introduces an additional non-pole component. Therefore, unlike the Flatté-type propagator forms, the K-matrix formalism does not define a unique line shape before the production parameters are specified in the amplitude fit.

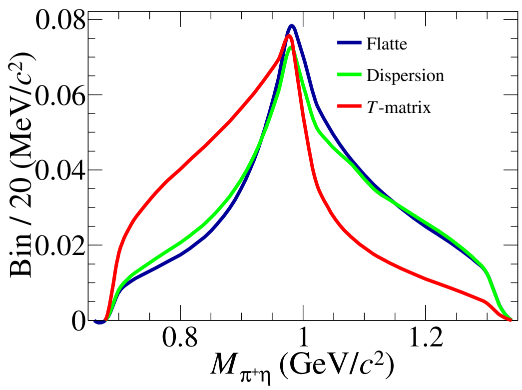

FIG. 1. Normalized $\pi^+\eta$ mass distributions obtained with the Flatté (blue), dispersively modified Flatté (green), and T-matrix (red) descriptions. Each distribution is normalized to unit area.

III. EVENT SELECTION

The BESIII detector and the upgraded multi-gap resistive plate chambers used in the time-of-flight systems are described in Refs. [18, 19] in detail, respectively. Since the D^+ and D^- are produced together in pairs, the double tag (DT) method [20] is employed to suppress backgrounds. Six tag channels $D^- \to K^+\pi^-\pi^-(\pi^0)$, $D^- \to K_S^0\pi^-(\pi^0)$, $D^- \to K_S^0\pi^-\pi^-\pi^+$, and $D^- \to K^+K^-\pi^-$ are used. Signal MC samples with $\psi(3770) \to D^+D^-$, $D^- \to$ tags and $D^+ \to \pi^+\eta\eta$ are generated, where the amplitude model from the fit to the data is used for the signal decay. The tracking, particle identification (PID), K_S^0, π^0, and η reconstruction are almost identical to those in Ref. [21], except for the signal window of invariant mass for η candidates, which is set to $0.45 < M(\gamma\gamma)_\eta < 0.65$ GeV/c^2 to improve the η reconstruction efficiency. Two variables, $M_{\rm BC} = \sqrt{E^2_{\rm beam} - |\vec{P}_{D^\pm}|^2}$ and $\Delta E = E_{D^\pm} - E_{\rm beam}$, are used to identify $D^\pm$ mesons, where $(E_{D^\pm}, \vec{P}_{D^\pm})$ is the four-momentum of the $D^\pm$ meson and $E_{\rm beam}$ is the beam energy. For both the tag and signal sides, any candidate with $M_{\rm BC} < 1.83$ GeV/c^2 or $|\Delta E| > 0.1$ GeV is first rejected. The candidate for each tag mode with $|\Delta E|$ closest to 0 is selected, while the signal candidate with $M_{\rm BC}$ closest to the D nominal mass [6] is chosen. Backgrounds are studied with an inclusive Monte Carlo (MC) sample simulated with GEANT4 [22], which includes all known open-charm decays, charmless decays and initial-state radiative decays to the J/ψ or $\psi(3686)$. All particle decays with known branching fractions are modeled with EVTGEN [23]. The remaining unknown charmonium decays are generated with LUNDCHARM [24].

For the tag channels, the $M_{\rm BC}$ signal windows are defined as ± 6 MeV/c^2 around the known D^- mass [6]; and the ΔE windows are set to 3.5 times the corresponding resolutions [21]. On the signal side, the $M_{\rm BC}$ signal window is required to be in the range [1.860, 1.880] GeV/c^2. Since the dominant background is from processes with no η in the final state, for events used in the amplitude analysis a multi-variant analysis (MVA) [25] is employed in which a Gradient Boosted Decision Tree (BDTG) classifier is developed based on the inclusive MC sample. The BDTG takes five discriminating variables: the natural logarithm of the χ^2 of constraining the two-photon pairs to the η mass; the invariant masses and the cosine of the helicity angles of the photon decaying from $\eta_{1,2}$ with higher energy, where the subscripts 1 and 2 for η represents a more or less energetic η. Studies of the MC samples show that a requirement on the output of the BDTG retains 78.3% signals and rejects 89.7% backgrounds. The possible distortion of the Dalitz-plot distribution due to this requirement is studied with MC samples and found to be negligible. A further requirement of $|\Delta E| < 0.040$ GeV is then imposed. Furthermore, to ensure all candidate events fall into the physical region of phase space, a kinematic fit is performed, where aside from four-momentum conservation, the invariant masses of $M(\gamma\gamma)_\eta$ and $M(\pi^+\eta\eta)_D$ are constrained to individual values quoted from the PDG [6]. Finally, a sample of 1624 candidates is retained with a purity of (85.1 ± 0.9)%.

IV. AMPLITUDE ANALYSIS FORMALISM

The amplitude analysis is performed using accepted events in data based on an unbinned maximum likelihood fit. The logarithm of the likelihood is constructed as

$$\ln\mathcal{L} = \ln(f_{\rm s}\tilde{S}(p) + (1-f_{\rm s})\tilde{B}(p)), \tag{16}$$

where $f_{\rm s}$ is the signal purity, p is the four-momenta of the final particles, and $\tilde{S}(p)$ and $\tilde{B}(p)$ are the probability density functions (PDFs) of the signal and background, respectively:

$$\begin{aligned}\tilde{S}(p) &= \frac{\epsilon(p)|\mathcal{M}(p)|^2 R_3(p)}{\int \epsilon(p)|\mathcal{M}(p)|^2 R_3(p)\mathrm{d}^3p},\\ \tilde{B}(p) &= \frac{\epsilon(p)B_\epsilon(p)R_3(p)}{\int \epsilon(p)B_\epsilon(p)R_3(p)\mathrm{d}^3p}.\end{aligned} \tag{17}$$

Here, $R_3(p)$ is the three-body phase space factor, and $\epsilon(p)$ is the efficiency function. The $\mathcal{M}(p)$ is the total amplitude of the signal, and $B_\epsilon(p)$ is the amplitude of the background. The background amplitude $B_\epsilon(p)$ is calculated with

$$B_\epsilon(p) = B(p)/\epsilon(p), \tag{18}$$

where the $B(p)$ is the function extracted from the inclusive MC sample with the signal removed and the $\epsilon(p)$ is the corresponding efficiency.

A. Signal amplitude formalism

The $\mathcal{M}(p)$ is modeled as the coherent sum of the amplitudes of all intermediate processes,

$$\mathcal{M}(p) = \sum_\alpha c_\alpha e^{i\phi_\alpha} A_\alpha, \tag{19}$$

where c_α and ϕ_α are the magnitude and phase of the $\alpha^{\rm th}$ amplitude, respectively. The amplitude A_α is defined as

$$A_\alpha = P_\alpha S_\alpha F^r_\alpha F^D_\alpha, \tag{20}$$

where P_α is the propagator for an intermediate resonance; S_α is the spin factor constructed with the covariant tensor formalism [26]. The four-momenta of the two identical η mesons are exchanged due to the Bose symmetry requirement. For a Dalitz plot of the decay $D^+ \to P_1P_2P_3$ ($P_{1,2,3}$ are the three decay products with $\mathrm{J^P} = 0^-$, in this paper, they are $\pi^+\eta\eta$), considering the decay chain of $D^+ \to RP_3$, $R \to P_1P_2$, two first-order operators are constructed as:

$$\begin{aligned}\tilde{T}^{(1)\mu}_D &= r^\mu_D - \frac{p_D \cdot r_D}{p^2_D} p^\mu_D,\\ \tilde{t}^{(1)}_{R\,\mu} &= r_{R\,\mu} - \frac{p_R \cdot r_R}{p^2_R} p^\mu_R,\end{aligned} \tag{21}$$

where p_D and p_R are the four-momenta of the D^+ and intermediate resonance R, respectively. $r_D = p_R - p_3$ and $r_R = p_1 - p_2$, $p_{1,2,3}$ are the four-momenta of the decay products. The two second-order operators are constructed as:

$$\begin{aligned}\tilde{T}^{(2)\mu\nu}_D &= \tilde{T}^{(1)\mu}_D \tilde{T}^{(1)\nu}_D - \frac{1}{3}\tilde{T}^{(1)}_D \cdot \tilde{T}^{(1)}_D (g^{\mu\nu} - \frac{p^\mu_D p^\nu_D}{p^2_D}),\\ \tilde{t}^{(2)}_{\mu\nu}(R) &= \tilde{t}^{(1)}_{R\,\mu}\tilde{t}^{(1)}_{R\,\nu} - \frac{1}{3}\tilde{t}^{(1)}_R \cdot \tilde{t}^{(1)}_R (g_{\mu\nu} - \frac{p_{R\,\mu}p_{R\,\nu}}{p^2_R}).\end{aligned} \tag{22}$$

Here, g is the metric tensor. Only the cases with orbital momentum L no more than 2 are considered due to the phase space limit. Then S_α is

$$S = \begin{cases} 1.0, & L = 0\\ \tilde{T}^{(1)\mu}_D \tilde{t}^{(1)}_{R\,\mu}, & L = 1\\ \tilde{T}^{(2)\mu\nu}_D \tilde{t}^{(2)}_{R\,\mu\nu}, & L = 2. \end{cases} \tag{23}$$

The F^r_α and F^D_α are the barrier factors for the intermediate state and D meson, respectively, which are

$$F = \begin{cases} 1.0, & L = 0\\ \sqrt{\frac{1+z_0}{1+z}}, & L = 1\\ \sqrt{\frac{9+3z_0+z_0^2}{9+3z+z^2}}, & L = 2. \end{cases} \tag{24}$$

Here, $z = (qr_e)^2$, for F^D, q is the momentum of R or P_3 at the rest frame of D^+ and r_e is the effective radii for D^+ and set to 5.0 GeV^{-1} in the nominal fit; for F^R, q is the momentum of P_1 or P_2 at the rest frame of R and r_e is the effective radii for R and set to 3.0 GeV^{-1} in the nominal fit.

The propagator P_α is taken to be a relativistic Breit-Wigner formula for all resonances except the $a_0(980)$, which considers the Flatté parameterization, dispersively modified Flatté parameterization, T-matrix formula and K-matrix formula.

B. Fit fraction and branching fraction of intermediate process

The fit fraction (FF) of the $\alpha^{\rm th}$ amplitude is calculated with

$$FF_\alpha = \frac{\int |c_\alpha A_\alpha(p)|^2 R_3(p) d^3p}{\int |M(p)|^2 R_3(p) d^3p}. \tag{25}$$

Here, it is noted that there is no efficiency function being incorporated. The branching fraction of the $\alpha^{\rm th}$ intermediate process is

$$\mathcal{B}_\alpha = \mathcal{B}(D^+ \to \pi^+\eta\eta) FF_\alpha, \tag{26}$$

V. SIGNAL MODEL CONSTRUCTION

In the Dalitz plot of $M^2(\pi^+\eta_a)$ versus $M^2(\pi^+\eta_b)$, shown in Fig. 2, a prominent band corresponding to the $a_0(980)^+$ resonance is observed in the $\pi^+\eta$ system, while no other clear structures are visible. Here, the subscripts a and b label the two identical η candidates, whose assignment is randomized on an event-by-event basis.

Motivated by this observation, the baseline signal model includes only the decay chain $D^+ \to a_0(980)^+\eta$, $a_0(980)^+ \to \pi^+\eta$. In each fit, this amplitude is chosen as the reference amplitude, with its magnitude and phase fixed to 1.0 and 0.0, respectively. The additional amplitudes listed in Table II are tested individually. The statistical significance of each additional amplitude is evaluated from the change in the log-likelihood and the change in the number of free parameters between the fits with

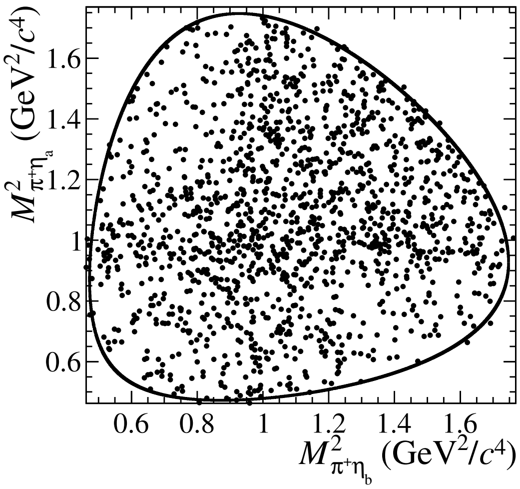

FIG. 2. Dalitz plot of $M^2(\pi^+\eta_a)$ versus $M^2(\pi^+\eta_b)$ for the selected $D^+ \to \pi^+\eta\eta$ candidates. The subscripts a and b label the two identical η candidates, whose assignment is randomized on an event-by-event basis. There are some events outside of the Dalitz boundary due to the detector resolution.

and without the amplitude. The subscripts V and T denote vector and tensor nonresonant amplitudes, respectively.

The tests are divided into four sets, according to the different $a_0(980)^+$ line shapes, described by:

A. the Flatté parameterization;

B. the dispersively modified Flatté parameterization;

C. the T-matrix formalism; and

D. the K-matrix formalism.

TABLE II. The additional amplitudes being considered, where the subscripts V and T represent the vector and tensor non-resonant states.

	Amplitude
I	$D^+ \to f_0(1370)\pi^+$, $f_0(1370) \to \eta\eta$
II	$D^+ \to f_0(1500)\pi^+$, $f_0(1500) \to \eta\eta$
III	$D^+ \to f_0(1710)\pi^+$, $f_0(1710) \to \eta\eta$
IV	$D^+ \to f_2(1270)\pi^+$, $f_2(1270) \to \eta\eta$
V	$D^+ \to f_2'(1525)\pi^+$, $f_2'(1525) \to \eta\eta$
VI	$D^+ \to f_2(1565)\pi^+$, $f_2(1565) \to \eta\eta$
VII	$D^+ \to f_2(1640)\pi^+$, $f_2(1640) \to \eta\eta$
VIII	$D^+ \to (\eta\eta)_T\pi^+$
IX	Constant term
X	$D^+ \to (\pi^+\eta)_V\eta$
XI	$D^+ \to a_2(1320)^+\eta$
XII	$D^+ \to (\pi^+\eta)_T\eta$

In the test sets A and B, the $a_0(980)$ parameters are fixed to the values reported in Refs. [14] and [15], respectively. In the test set C, the T-matrix amplitude is used as described in Sec. II, without introducing additional free parameters. In the test set D, the scattering part of the K-matrix formalism is fixed: the bare masses, channel couplings, and smooth-background parameters of the K-matrix are taken from Table I of Ref. [13]. The production-vector parameters, which describe the coupling of the initial D^+ decay to the K-matrix bare poles and smooth non-pole production terms, are treated as free fit parameters. In the test sets A–D, the amplitude "IX. Constant term" represents a uniform nonresonant amplitude over phase space. When this term is included together with the dominant $a_0(980)^+\eta$ amplitude, the fitted solution exhibits a large constructive interference, exceeding 30%. Such a large interference indicates a strong correlation between the constant term and the $a_0(980)^+\eta$ amplitude, which makes the separation of the two contributions unstable and model dependent. Therefore, the constant term is not included as an independent component in the nominal signal model.

A. Test set A: Flatté parameterization

The baseline model gives $\ln\mathcal{L} = 105.3$ and $\chi^2/\mathrm{NDOF} = 161.1/92$. Throughout this paper, the $M(\pi^+\eta)$ projection is obtained by filling both $M(\pi^+\eta_a)$ and $M(\pi^+\eta_b)$ combinations for each event, in order to reduce statistical fluctuations. The projections of $M(\pi^+\eta)$ and $M(\eta\eta)$ are shown in Fig. 3. The observed $a_0(980)$ line shape is not well reproduced by the baseline model.

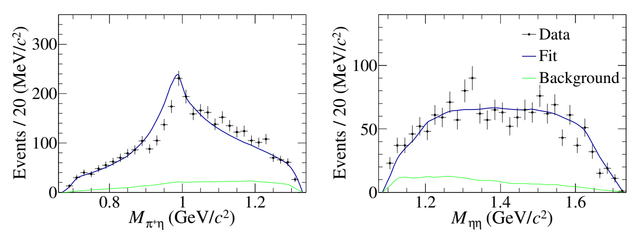

FIG. 3. The projections of (left) $M(\pi^+\eta)$ and (right) $M(\eta\eta)$ for the baseline model with Flatté parameterization for $P_{a_0(980)}$. The black dots with error bars are the data; the blue lines are the total fit; and the green lines are the background.

The additional amplitudes listed in Table II are then tested by adding them individually to the baseline model. The values of $\ln\mathcal{L}$, fit qualities, and significances relative to the baseline model are summarized in Table III.

As given in Table III, adding a single additional amplitude improves the fit quality in some cases, but none of these models provides a satisfactory description of

TABLE III. The fit qualities for the fits after adding one additional amplitude in the baseline model. The significance is calculated relative to the baseline model.

Amplitude	$\ln\mathcal{L}$	χ^2/NDOF	Significance (σ)
I	108.0	146.1/92	1.9
II	112.3	157.3/92	3.3
III	113.0	141.8/92	3.5
IV	112.9	143.7/92	3.5
V	119.9	136.0/92	5.0
VI	123.0	128.1/92	5.6
VII	123.4	133.5/92	5.7
VIII	116.8	134.0/92	4.4
IX	133.3	106.6/92	7.2
X	107.3	146.6/92	1.5
XI	116.5	152.1/92	4.3
XII	110.1	158.6/92	2.7

the data. The largest improvement is obtained for the constant term; however, as discussed above, this term is strongly correlated with the dominant $a_0(980)^+\eta$ amplitude and does not provide a stable independent contribution. The single-amplitude tests give significances above 5σ for the tensor states $f_2'(1525)$, $f_2(1565)$, and $f_2(1640)$. The projections for the three tensor amplitudes that give the largest improvements in the direct-production tests are shown in Fig. 4. The complete set of projections for all tested additional amplitudes in the Flatté case is provided in Fig. 15 of Appendix A. However, no corresponding peak-like structures are observed in the $M(\eta\eta)$ projection. Since these tensor states populate the same high-$M(\eta\eta)$ region and have partially overlapping line shapes, their apparent significances in the single-amplitude tests can be enhanced by correlations with the dominant $a_0(980)^+\eta$ amplitude and with each other.

The interpretation of the $f_2'(1525)$ contribution is further constrained by existing information from $D^+ \to K^-K^+\pi^+$. Using the branching fractions for $f_2'(1525) \to \eta\eta$ and $f_2'(1525) \to K\bar{K}$, together with the FFs obtained in the present fit, one would expect a corresponding contribution in $D^+ \to K^-K^+\pi^+$ at the percent level. Such a contribution is not supported by previous Dalitz-plot analyses of $D^+ \to K^-K^+\pi^+$ [27, 28]. This comparison suggests that the large significance obtained for $f_2'(1525)$ in the single-amplitude test is likely driven by correlations and should not be interpreted as evidence for an independent $f_2'(1525)\pi^+$ component.

A consistency check is also performed for the $f_2(1270)$ contribution. Using the PDG branching fractions $\mathcal{B}(D^+ \to f_2(1270)\pi^+, f_2(1270) \to \pi^+\pi^-)$, $\mathcal{B}(f_2(1270) \to \pi\pi)$, $\mathcal{B}(f_2(1270) \to \eta\eta)$ and $\mathcal{B}(D^+ \to \pi^+\eta\eta)$, the expected FF for $D^+ \to f_2(1270)\pi^+$, $f_2(1270) \to \eta\eta$ is estimated to be $(1.1 \pm 0.2) \times 10^{-3}$. When the FF is fixed to this value in the fit including amplitude IV, the significance of the $f_2(1270)$ contribution is reduced to below 3σ.

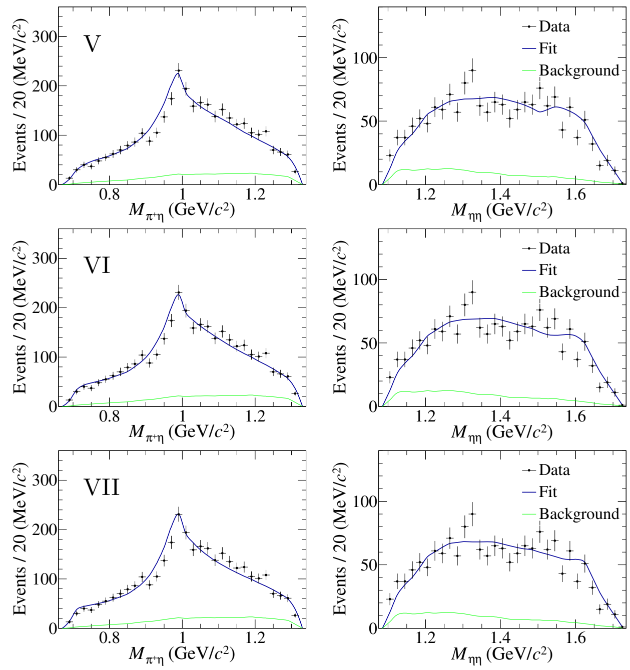

FIG. 4. The same as Fig. 3, but for the direct-production models including one additional tensor amplitude V. $f_2(1270)$, VI. $f_2'(1525)$, and VII. $f_2(1640)$ with the Flatté parameterization for $P_{a_0(980)}$.

TABLE IV. The fit qualities for the fits with models adding two additional f_2 states in the baseline model are listed. The significance is calculated with comparing with the baseline plus single f_2 states.

Amplitude	$\ln\mathcal{L}$	χ^2/NDOF	Significance (σ)		
			V	VI	VII
V + VI	127.7	119.1/92	2.6	3.6	-
V + VII	126.2	126.6/92	1.9	-	3.1
VI + VII	124.7	127.7/92	-	1.1	1.3

To further examine correlations among the tensor components, three fits are performed by including two of the three tensor states $f_2'(1525)$, $f_2(1565)$, and $f_2(1640)$ simultaneously. The projections are shown in Fig. 5, and the fit results are summarized in Table IV. The significance of each tensor state is evaluated from the change in $\ln\mathcal{L}$ with respect to the corresponding fit containing only the other tensor state.

As shown in Table IV, the incremental significances of the tensor states are substantially smaller than those obtained in the single-amplitude tests. When all three tensor states are included simultaneously, the fit gives $\ln\mathcal{L} = 128.4$ and $\chi^2/\mathrm{NDOF} = 120.2/92$, indicating only a marginal improvement. These results confirm that the apparent tensor contributions are strongly correlated and

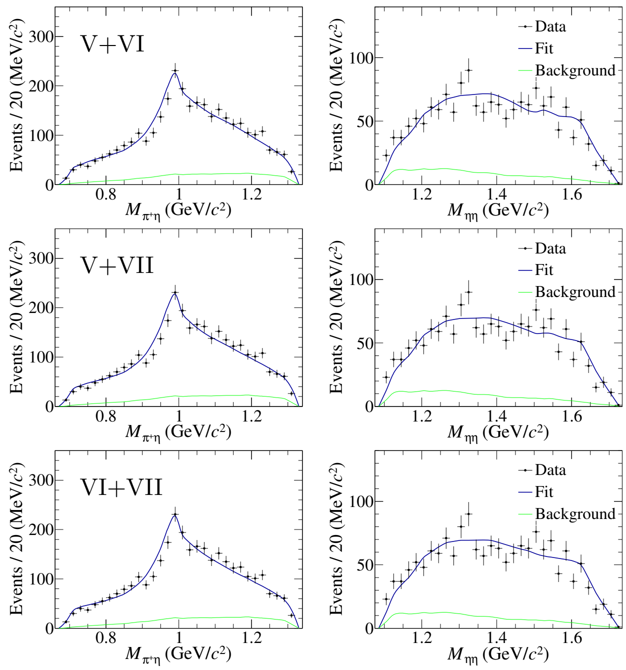

FIG. 5. The same as Fig. 3, but for the models after further considering (top) $f_2'(1525) + f_2(1565)$, (middle) $f_2'(1525) + f_2(1640)$, and (bottom) $f_2(1565) + f_2(1640)$.

do not provide stable independent components.

Since the single-amplitude test with $f_2(1565)$ gives the best fit quality among the three tensor-state candidates, it is used as the reference model for further tests of additional components. Additional tests are performed by adding each of the remaining amplitudes, except for the constant term, to the model "baseline+$f_2(1565)$". The largest value of $\ln\mathcal{L}$ is 127.3, and the best fit quality is $\chi^2/\mathrm{NDOF} = 113.4/92$, obtained with the model "baseline+$f_2(1565) + f_0(1710)$". Relative to the "baseline+$f_2(1565)$" model, the improvement corresponds to only 2.5σ. Moreover, the improvement is mainly associated with a large interference between the $f_0(1710)$ and $a_0(980)^+\eta$ amplitudes. For the other tested models, $\ln\mathcal{L}$ remains below 127.0 and the fit quality is worse than $\chi^2/\mathrm{NDOF} = 119.5/92$.

Based on these studies, we conclude that the discrepancy between the data and the baseline Flatté model cannot be resolved by adding small conventional resonant or non-resonant amplitudes.

B. Test set B: dispersively modified Flatté parameterization

As discussed in Sec. V A, the discrepancy between the data and the Flatté baseline model cannot be resolved by adding the conventional additional amplitudes listed in Table II. The baseline fit gives $\ln\mathcal{L} = 112.0$ and $\chi^2/\mathrm{NDOF} = 162.7/92$. The corresponding projections are shown in Fig. 6.

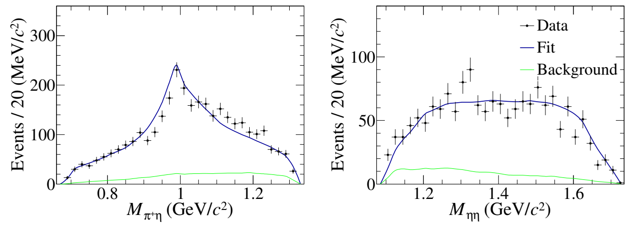

FIG. 6. The same as Fig. 3, but for the baseline model using the dispersively modified Flatté parameterization.

The twelve additional amplitudes listed in Table II are then tested by adding them individually to the dispersive baseline model. The corresponding projections are shown in Fig. 16 of Appendix A. The values of $\ln\mathcal{L}$, fit qualities, and significances relative to the baseline model are summarized in Table V. The largest improvement is obtained for model IX, the constant term. However, as in the test set A, this term produces a large interference with the dominant $a_0(980)^+\eta$ amplitude and is therefore not included as an independent component in the nominal signal model. For the remaining fits, the mismatch in the $M(\pi^+\eta)$ spectrum persists.

TABLE V. Fit results for models obtained by adding one additional amplitude to the dispersive baseline model. The significance is evaluated relative to the baseline model.

Amplitude	$\ln\mathcal{L}$	χ^2/NDOF	Significance(σ)
I	117.9	136.9/92	2.9
II	114.6	156.1/92	1.7
III	125.1	125.9/92	4.7
IV	120.8	143.6/92	3.7
V	119.5	147.6/92	3.4
VI	123.8	138.6/92	4.4
VII	124.0	143.4/92	4.5
VIII	122.6	130.1/92	4.2
IX	133.1	105.4/92	6.1
X	116.7	142.5/92	2.5
XI	114.0	164.5/92	1.4
XII	112.1	162.6/92	0.1

Compared with the Flatté baseline model, the dispersive baseline model has a larger likelihood value. Consequently, the relative improvements obtained by adding the f_0 and f_2 amplitudes are reduced, and none of these resonant amplitudes reaches a significance above 5σ. Among the resonant amplitudes, the largest improvement is obtained when the $f_0(1710)\pi^+$ amplitude is added. In this fit, the FF of the $f_0(1710)\pi^+$ contribution is $(1.3 \pm 0.6)\%$, while the associated interference fraction is $(-4.3 \pm 3.8)\%$. Since no clear corresponding structure is observed in the $M(\eta\eta)$ projection, this contribution is not considered to provide a stable independent component and is not adopted in the nominal signal model.

As in Sec. V A, further tests are performed using the model "baseline+$f_2(1565)$" as the reference, because it gives the best fit quality among the single-amplitude resonant additions in this test set. Additional amplitudes, except for the constant term, are then added individually to this reference model. The largest likelihood value, $\ln\mathcal{L} = 129.5$, is obtained for the model "baseline+$f_2'(1525) + f_2(1565)$", with $\chi^2/\mathrm{NDOF} = 128.6/92$. Relative to the corresponding single-f_2 models, the incremental significances of the $f_2'(1525)$ and $f_2(1565)$ contributions are 2.9σ and 4.1σ, respectively. This behavior is similar to that observed in the test set A and indicates that the apparent tensor contributions are strongly correlated rather than stable independent components.

Based on these studies, we conclude that the discrepancy between the data and the dispersive baseline model cannot be resolved by adding small conventional resonant or nonresonant amplitudes.

C. Test set C: T-matrix formalism

In the test set C, the $\pi\eta$ S-wave dominated by the $a_0(980)$ contribution is described by the fixed T-matrix amplitude introduced in Sec. II. The baseline fit gives $\ln\mathcal{L} = 67.9$ and $\chi^2/\mathrm{NDOF} = 278.7/92$. The corresponding projections are shown in Fig. 7. Compared with the Flatté and dispersively modified Flatté baseline fits in Secs. V A and V B, this fit gives a substantially worse description of the data.

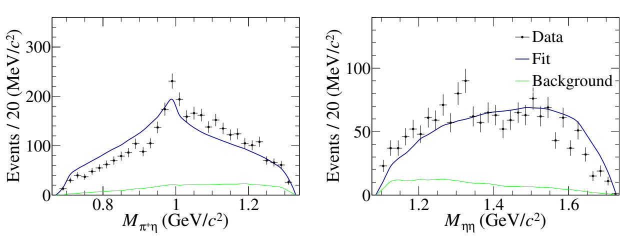

FIG. 7. The same as Fig. 3, but for the baseline model using the fixed T-matrix description of the $\pi\eta$ S-wave.

The additional amplitudes listed in Table II are then tested by adding them individually to the T-matrix baseline model. The corresponding projections are shown in Fig. 17 of Appendix A, and the fit results are summarized in Table VI. Because the T-matrix baseline model gives a poor description of the data, several additional amplitudes lead to large apparent improvements in $\ln\mathcal{L}$. However, these improvements should not be interpreted as evidence for independent physical contributions since the fit quality of the corresponding baseline model are much worse than those using Flatté and dispersively modified Flatté parameterizations for $P_{a_0(980)}$. Furthermore, the large contributions given by these tests disagree with those presented in sections V A and V B, and the independent Dalitz plot analyses for the decay $D^+ \to K^-K^+\pi^+$ [27, 28].

TABLE VI. Fit results for models obtained by adding one additional amplitude to the T-matrix baseline model.

Amplitude	$\ln\mathcal{L}$	χ^2/NDOF	Significance
I	106.8	179.2/92	8.5
II	79.6	251.5/92	4.4
III	113.1	172.0/92	9.2
IV	93.7	208.7/92	6.8
V	81.6	245.0/92	4.8
VI	92.4	223.9/92	6.6
VII	94.5	228.7/92	7.0
VIII	94.0	207.4/92	6.9
IX	127.3	130.4/92	10.7
X	88.5	223.3/92	6.0
XI	77.2	231.3/92	3.9
XII	79.9	234.5/92	4.5

In particular, the models "baseline+III" and "baseline+IX" exhibit large interference with the dominant $\pi\eta$ S-wave amplitude. These solutions are therefore not considered stable independent descriptions of the data. For the remaining models, although the likelihood values are improved relative to the T-matrix baseline, the fit qualities remain poor and the mismatch in the $M(\pi^+\eta)$ spectrum persists. Since the baseline T-matrix description is already strongly disfavored, the large significances obtained for several additional amplitudes mainly reflect their ability to compensate for the poor $\pi\eta$ line shape description. They are therefore not interpreted as evidence for genuine additional intermediate states.

Additional tests including more than one extra amplitude show similar behavior: the improvements are mainly driven by strong correlations and interference effects rather than by well-resolved structures in the data. Therefore, the fixed T-matrix description, even when supplemented with conventional resonant or nonresonant amplitudes, does not provide a satisfactory description of the data.

D. Test set D: K-matrix formalism

In this section, the $\pi\eta$ S-wave dominated by the $a_0(980)$ contribution is described with the K-matrix formalism. The scattering part of the K-matrix is fixed to the four parameter sets reported in Ref. [13], denoted as s1–s4 and listed in Table I. For each of the parameter set, the production-vector parameters are determined from the fit. In the baseline fits, the parameter s_1^{prod} is found to be consistent with zero within its uncertainty and becomes poorly constrained when allowed to float. It is therefore fixed to zero in all subsequent fits.

The fitted production-vector parameters, together with the corresponding $\ln\mathcal{L}$ and χ^2/NDOF values, are listed in Table VII. The projections are shown in Fig. 8.

TABLE VII. Fit results for the K-matrix baseline models using the four parameter sets. The production-vector parameters β_2 and f_1^{prod} are determined from the fit.

Parameter set	β_2	f_1^{prod}	$\ln\mathcal{L}$	χ^2/NDOF
s1	-7.1 ± 1.0	0.63 ± 0.13	84.8	159.1/92
s2	-9.5 ± 1.3	0.47 ± 0.10	92.9	158.3/92
s3	-9.9 ± 1.3	1.06 ± 0.18	66.6	185.2/92
s4	-16.0 ± 1.9	1.07 ± 0.16	75.0	180.8/92

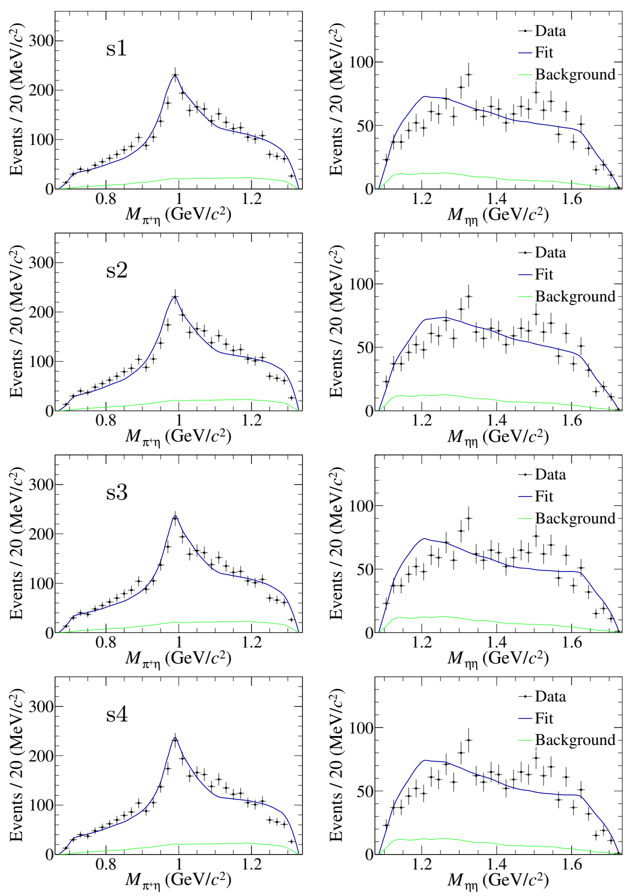

FIG. 8. The same as Fig. 3, but for the fit model using the K-matrix form to parameterize the $a_0(980)$ with the parameter sets (top) s1, (second row) s2, (third row) s3 and (bottom) s4.

As an alternative description of the smooth production term, the form in Eq. 12 is replaced by the first-order polynomial form in Eq. 13. The fitted values of β_2, $c_{1,0}$, and $c_{1,1}$, together with the corresponding $\ln\mathcal{L}$ and χ^2/NDOF values, are listed in Table VIII. The projections are shown in Fig. 9. This alternative form does not lead to a satisfactory improvement in the fit quality.

TABLE VIII. Fit results for the K-matrix baseline models with the smooth production term in the P vector replaced by a first-order polynomial.

Parameter set	β_2	$c_{1,0}$	$c_{1,1}$	$\ln\mathcal{L}$	χ^2/NDOF
s1	-10.4 ± 2.5	2.04 ± 0.44	-0.28 ± 0.37	83.5	164.3/92
s2	-6.6 ± 1.6	1.44 ± 0.32	-1.05 ± 0.27	91.0	154.2/92
s3	-25.1 ± 5.2	4.38 ± 0.85	0.66 ± 0.65	77.9	179.4/92
s4	-18.5 ± 2.8	3.09 ± 0.51	-0.95 ± 0.39	74.3	183.1/92

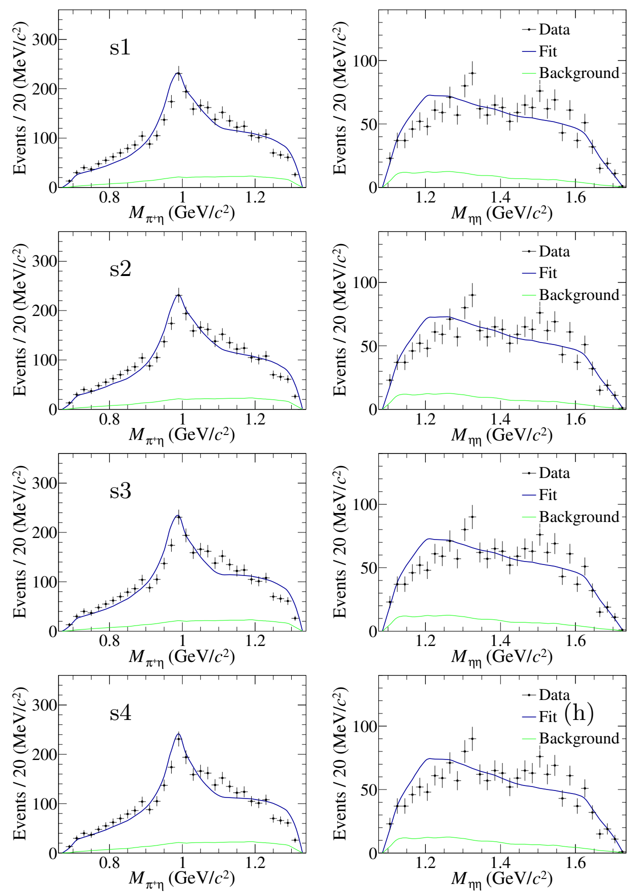

FIG. 9. The same as Fig. 8, but for the fit model with an altered P-vector background term.

Among the baseline fits, the parameter set s2 gives the best fit quality and is therefore used for the subsequent tests with additional amplitudes. The additional amplitudes listed in Table II are added individually to the K-matrix baseline model. The corresponding fit results are summarized in Table IX, and the projections are shown in Fig. 18 of Appendix A.

Similar to the behavior observed in the test set C, the models "baseline+III", "baseline+IX", and "base-

TABLE IX. Fit results for models obtained by adding one additional amplitude to the K-matrix baseline model with the parameter set s2.

Amplitude	β_2	$f_1^{\rm prod}$	$\ln\mathcal{L}$	χ^2/NDOF	Significance
I	-14.0 ± 1.9	0.53 ± 0.11	112.4	137.4/92	5.9
II	-12.0 ± 1.6	0.59 ± 0.10	120.2	135.7/92	7.1
III	-7.5 ± 1.5	0.01 ± 0.12	131.9	114.6/92	8.6
IV	-9.9 ± 1.5	0.56 ± 0.11	104.4	140.1/92	4.4
V	-7.7 ± 1.5	0.37 ± 0.11	102.7	146.5/92	4.0
VI	-8.6 ± 1.8	0.47 ± 0.14	104.7	145.3/92	4.5
VII	-8.6 ± 2.0	0.46 ± 0.17	101.9	155.2/92	3.8
VIII	-14.3 ± 2.4	0.98 ± 0.19	106.6	136.6/92	4.9
IX	-33.3 ± 12.4	0.30 ± 0.24	142.7	90.9/92	9.6
X	-26.2 ± 4.1	0.87 ± 0.24	139.7	98.1/92	9.4
XI	-9.0 ± 1.8	0.41 ± 0.14	102.2	141.2/92	3.9
XII	-16.3 ± 4.1	0.98 ± 0.32	97.2	151.7/92	2.4

line+X", corresponding to the additional $f_0(1710)\pi^+$ amplitude, the constant term, and the $(\pi^+\eta)_V\eta$ amplitude, respectively, exhibit large interference with the dominant $\pi\eta$ S-wave amplitude. These solutions are therefore not considered stable independent descriptions of the data. For the remaining amplitudes with large apparent significances, no corresponding clear structures are observed in the relevant invariant-mass projections. As in the previous test sets, these apparent improvements are mainly driven by correlations with the dominant $\pi\eta$ S-wave amplitude rather than by well-resolved additional components.

Therefore, the K-matrix formalism with the reference scattering parameters, even with alternative production-vector forms or additional conventional amplitudes, does not provide a satisfactory description of the data.

E. Signal model conclusion

The studies in Secs. V A–V D show that the discrepancy between the data and the baseline descriptions cannot be resolved by adding the conventional resonant or non-resonant amplitudes listed in Table II. Although some additional amplitudes lead to sizable improvements in the likelihood, their fitted contributions are not stable. In particular, their significances change substantially when more than one additional amplitude is included, and several of the apparent improvements are accompanied by large interference with the dominant $\pi\eta$ S-wave amplitude. Moreover, no clear corresponding structures are observed in the relevant invariant-mass projections.

This conclusion is consistent across the Flatté, dispersively modified Flatté, T-matrix, and K-matrix descriptions tested above. The large significances obtained for some amplitudes in the test sets C and D mainly reflect the poor description of the dominant $\pi\eta$ line shape in the corresponding baseline models. They are therefore not interpreted as evidence for genuine additional intermediate states. Based on these studies, no additional amplitude is included as an independent component in the nominal signal model. The nominal signal model contains only the decay chain $D^+ \to a_0(980)^+\eta$, $a_0(980)^+ \to \pi^+\eta$.

VI. FURTHER AMPLITUDE-ANALYSIS TESTS

To improve the description of the data, further tests are performed by allowing the $a_0(980)$ parameters to float in the amplitude fit. Two cases are considered:

- floating the $a_0(980)$ parameters in the Flatté parameterization;
- floating the $a_0(980)$ parameters in the dispersively modified Flatté parameterization.

Due to the limited statistics and the weak sensitivity to the $\pi\eta'$ channel, the coupling constant $g_{\pi\eta'}$ is fixed to the values reported in Refs. [14] and [15] for the Flatté and dispersively modified Flatté parameterizations, respectively. We do not attempt to float the scattering parameters of the K matrix, since they are constrained by coupled-channel scattering information and cannot be reliably determined from the present single decay channel alone.

For the Flatté and dispersively modified Flatté parameterizations, the corresponding pole positions, $\sqrt{s}_{\rm pole}$, are also determined. The pole position is a process-independent quantity that characterizes the resonance. It is written as $\sqrt{s}_{\rm pole} = M_{\rm pole} - i\Gamma_{\rm pole}/2$, where $M_{\rm pole}$ and $\Gamma_{\rm pole}$ are the pole mass and width, respectively. For the $a_0(980)$, the pole is expected to be located on an unphysical sheet close to the physical region and near the $K\bar{K}$ threshold [6].

For each decay channel j, the right-hand branch cut starts at the threshold $s_j^+ = (m_{j1} + m_{j2})^2$ and extends to $+\infty$ along the real axis. The left-hand cuts are not considered in the sheet classification. Two branches of the phase-space factor are defined as

$$\rho_j^{\lambda_j}(s) = \lambda_j \rho_j^+(s), \qquad \lambda_j = \pm, \tag{27}$$

where

$$\rho_j^+(s) = \frac{1}{s}\sqrt{(s - s_j^+)(s - s_j^-)}, \qquad s_j^\pm = (m_{j1} \pm m_{j2})^2. \tag{28}$$

Here, m_{j1} and m_{j2} are the masses of the two particles in channel j. The physical branch is chosen by approaching the physical axis from the upper half-plane.

For the $a_0(980)$, three coupled channels are considered: $\pi\eta$, $K\bar{K}$, and $\pi\eta'$, giving $2^3 = 8$ Riemann sheets. A sheet is labelled by the signs $(\lambda_{\pi\eta}, \lambda_{K\bar{K}}, \lambda_{\pi\eta'})$, and the physical sheet is $(+++)$. The unphysical sheets closest to the physical region are $(-++)$, $(--+)$, and $(---)$. For the CLEO Flatté parameters, $g_{\pi\eta'} = 0$, so the $\pi\eta'$ channel is decoupled from the denominator. In this case, the third sheet label is immaterial, and the sheet $(-++)$ is equivalent to the two-channel sheet $(-+)$ in the $(\pi\eta, K\bar{K})$ space. Following Ref. [29], the pole search is performed on the relevant nearby sheets.

Denoting the denominator of the $a_0(980)$ dynamical function by $D_{a_0}(s)$, poles are obtained by solving

$$D_{a_0}^{\lambda_{\pi\eta},\lambda_{K\bar{K}},\lambda_{\pi\eta'}}(s) = 0 \tag{29}$$

on the corresponding Riemann sheets. The pole associated with the $a_0(980)$ is expected to be close to the $K\bar{K}$ threshold. In the present study, the search is focused on the $(-++)$ and $(--+)$ sheets. Poles found on the $(--+)$ sheet have much larger imaginary parts and are far from the near-threshold region relevant to the $a_0(980)$. Therefore, only poles on the $(-++)$ sheet are reported.

With the nominal $a_0(980)$ parameters reported by CLEO [14] and the Flatté parameterization, the pole position is found to be

$$\sqrt{s}_{\text{pole}} = (1.022 - i\,0.070)\ \text{GeV}/c^2. \tag{30}$$

With the nominal $a_0(980)$ parameters reported by BESIII [15] and the dispersively modified Flatté parameterization, the pole position is

$$\sqrt{s}_{\text{pole}} = (1.046 - i\,0.064)\ \text{GeV}/c^2. \tag{31}$$

A. Floating the $a_0(980)$ parameters in the Flatté parameterization

As discussed in Sec. V, the nominal signal model contains only the decay chain $D^+ \to a_0(980)^+\eta$, $a_0(980)^+ \to \pi^+\eta$. We first use this baseline model and leave the Flatté parameters free. Since the value of M_0 reported in Ref. [14] is much more precisely determined than the coupling constants $g^2_{\pi\eta}$ and $g^2_{K\bar{K}}$, only the two coupling constants are floated in the first step, while M_0 is fixed to the CLEO value. The fit gives $\ln\mathcal{L} = 109.3$, $g^2_{\pi\eta} = (0.449 \pm 0.038)\ \text{GeV}^2/c^4$, and $g^2_{K\bar{K}} = (0.371 \pm 0.098)\ \text{GeV}^2/c^4$, with $\chi^2/\text{NDOF} = 158.8/92$. The corresponding projections are shown in Fig. 10. The data are still not well described.

A further fit is performed by also floating M_0. The fit returns $M_0 = (1.082 \pm 0.017_{\text{stat}})\ \text{GeV}/c^2$, $g^2_{\pi\eta} = (0.469 \pm 0.047_{\text{stat}})\ \text{GeV}^2/c^4$, and $g^2_{K\bar{K}} = (0.566 \pm 0.149_{\text{stat}})\ \text{GeV}^2/c^4$. The fit gives $\ln\mathcal{L} = 142.5$ and $\chi^2/\text{NDOF} = 85.4/92$. The projections are shown in Fig. 11.

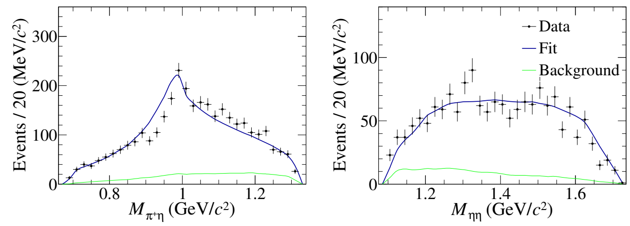

FIG. 10. The same as Fig. 3, but for baseline fit by floating the $a_0(980)$ coupling constants with using Flatté parameterization for $P_{a_0(980)}$.

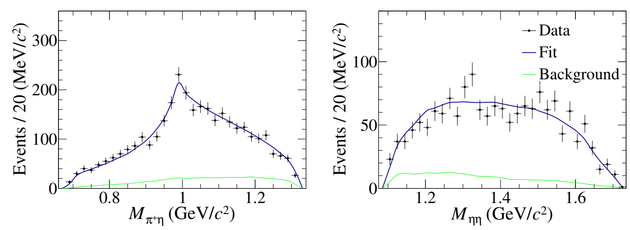

FIG. 11. The same as Fig. 3, but for baseline fit by floating all the $a_0(980)$ parameters with using Flatté parameterization for $P_{a_0(980)}$.

Although the data are well described after floating all three Flatté parameters, the resulting parameters differ significantly from the CLEO values. The corresponding pole position is $\sqrt{s}_{\text{pole}} = [(1.096 \pm 0.015_{\text{stat}}) - i(0.042 \pm 0.024_{\text{stat}})]\ \text{GeV}/c^2$. The pole mass is therefore shifted well above the $K\bar{K}$ threshold, which is unexpected for the near-threshold $a_0(980)$ state.

To examine whether this pole shift can be attributed to systematic effects, systematic uncertainties on the floated parameters and pole position are evaluated. The following sources are considered. The detailed results are summarized in Table X.

(I) The fixed value of $g_{\pi\eta'}$ is varied within the uncertainty reported in Ref. [14].

(II) The signal purity f_s is varied within its uncertainty to estimate the effect of the background fraction.

(III) The uncertainty due to the background shape includes three contributions: the choice of the ΔE window used to select the background sample, the kernel bandwidth used in extracting the background shape, and the statistical fluctuation of the background sample. The last contribution is estimated with the bootstrap method [30, 31].

(IV) The uncertainty due to the fit bias is obtained from the input-output (IO) check described in Sec. VI A 1.

(V) The uncertainty associated with the reconstruction efficiency includes tracking, PID, and η reconstruction.

(VI) The uncertainty due to possible additional amplitudes is evaluated by repeating the fit with each additional amplitude considered in Table II, except for the constant term. For each parameter, the largest deviation from the nominal result is assigned as the systematic uncertainty from this source.

TABLE X. Systematic uncertainties for the $a_0(980)$ parameters and pole position obtained with the Flatté parameterization. The values are given in units of 10^{-2}, with mass-related quantities in GeV$/c^2$ and coupling constants in GeV$^2/c^4$.

Parameter	I	II	III	IV	V	VI	Total
M_0	0.1	0.3	0.7	0.2	0.1	2.5	2.6
$g^2_{\pi\eta}$	0.4	0.6	2.2	0.5	0.0	6.0	6.4
$g^2_{K\bar{K}}$	0.9	1.2	6.4	0.9	0.1	14.2	15.6
$M_{\rm pole}$	0.0	0.2	0.6	0.1	0.1	1.7	1.8
$\Gamma_{\rm pole}/2$	0.2	0.1	0.9	0.1	0.0	3.7	3.8

Based on the systematic study, the final pole mass is

$$M_{\rm pole} = (1.096 \pm 0.015_{\rm stat} \pm 0.018_{\rm syst})\ {\rm GeV}/c^2. \tag{32}$$

The difference between this $M_{\rm pole}$ and the pole mass calculated from the CLEO parameters cannot be covered by the systematic uncertainty. Thus, although floating the Flatté parameters improves the fit quality, it drives the pole mass well above the near-threshold region expected for the $a_0(980)$.

1. IO check

The IO check is performed using 300 data-sized MC samples. In these samples, the signal process is generated according to the amplitude model $D^+ \to a_0(980)^+\eta$, $a_0(980)^+ \to \pi^+\eta$, with the $a_0(980)$ parameters set to the values obtained from data. The same event-selection and amplitude-analysis procedures as those used for data are applied to these MC samples.

For each parameter, the pull is defined as

$${\rm pull} = \frac{V_{\rm out} - V_{\rm in}}{\sigma_{\rm out}}, \tag{33}$$

where $V_{\rm out} \pm \sigma_{\rm out}$ is the fitted result from a pseudoexperiment, and $V_{\rm in}$ is the generated input value. The pull distributions obtained from the 300 samples are fitted with Gaussian functions. The fitted mean, μ_p, is used to evaluate possible fit bias, while the fitted width, σ_p, is used to check whether the statistical uncertainty is properly estimated.

If μ_p differs significantly from zero, the fitted value in data is corrected according to

$$V_c = V - \mu_p \sigma_{\rm stat}, \tag{34}$$

where $V \pm \sigma_{\rm stat}$ is the result obtained from data and V_c is the corrected value. The uncertainty associated with this correction is assigned as

$$\sigma_{\rm bias} = \sigma_{\mu_p}\, \sigma_{\rm stat}, \tag{35}$$

where σ_{μ_p} is the uncertainty of the fitted pull mean. If no significant bias is observed, no correction is applied, and the possible residual bias is assigned as a systematic uncertainty,

$$\sigma_{\rm bias} = \sqrt{\mu_p^2 + \sigma_{\mu_p}^2}\, \sigma_{\rm stat}. \tag{36}$$

If σ_p is larger than unity by more than three standard deviations, an additional systematic uncertainty is assigned to account for the possible underestimation of the statistical uncertainty:

$$\sigma_c = \sqrt{\sigma_p^2 - 1}\, \sigma_{\rm stat}. \tag{37}$$

The results of the IO checks are listed in Table XI.

TABLE XI. IO check results for the $a_0(980)$ parameters and pole quantities obtained with the Flatté parameterization.

Parameter	μ_p	σ_p
M_0	-0.11 ± 0.06	1.02 ± 0.04
$g^2_{\pi\eta}$	0.10 ± 0.06	0.97 ± 0.04
$g^2_{K\bar{K}}$	-0.30 ± 0.06	1.12 ± 0.05
$M_{\rm pole}$	-0.01 ± 0.06	0.97 ± 0.04
$\Gamma_{\rm pole}/2$	0.37 ± 0.06	0.95 ± 0.04

For M_0, $g^2_{\pi\eta}$, and $M_{\rm pole}$, no significant fit bias is observed from the fitted values of μ_p. Corrections are applied to $g^2_{K\bar{K}}$ and $\Gamma_{\rm pole}/2$, for which the fitted pull means deviate significantly from zero. The corrected results are $g^2_{K\bar{K},c} = (0.610 \pm 0.149_{\rm stat} \pm 0.156_{\rm syst})$ GeV$^2/c^4$ and $\Gamma_{{\rm pole},c}/2 = (0.033 \pm 0.024_{\rm stat} \pm 0.038_{\rm syst})$ GeV$/c^2$.

2. Tests with additional amplitudes in the floating Flatté fit

The same additional amplitudes as those considered in Sec. V A are tested in the floating-parameter Flatté fit. The constant term is excluded from these tests, following the discussion in Sec. V A. For each additional amplitude, the fit is repeated with M_0, $g^2_{\pi\eta}$, and $g^2_{K\bar{K}}$ allowed to float. The resulting $\ln\mathcal{L}$ values, fit qualities, significances of the additional amplitudes, and shifts in the fitted $a_0(980)$ parameters and pole position are summarized in Table XII. Here, "NA" indicates that no pole associated with the $a_0(980)$ is found on the $(-++)$ sheet; such fits are not used in the evaluation of the systematic uncertainty from additional amplitudes.

TABLE XII. Fit results obtained by adding one additional amplitude to the floating-parameter Flatté baseline model. The constant term is not included. All shifts are relative to the baseline fit with all Flatté parameters floated. The shifts are given in units of 10^{-2}, with GeV/c^2 for ΔM_0, ΔM_{pole}, and $\Delta(\Gamma_{\mathrm{pole}}/2)$, and GeV$^2/c^4$ for $\Delta g^2_{\pi\eta}$ and $\Delta g^2_{K\bar{K}}$. Here, "NA" indicates that no pole associated with the $a_0(980)$ is found on the $(-++)$ sheet.

Amplitude	$\ln\mathcal{L}$	χ^2/NDOF	Sig. (σ)	ΔM_0	$\Delta g^2_{\pi\eta}$	$\Delta g^2_{K\bar{K}}$	ΔM_{pole}	$\Delta(\Gamma_{\mathrm{pole}}/2)$
I	143.8	86.0/92	1.1	+2.1	+1.1	+13.4	+1.3	+2.6
II	146.1	83.6/92	2.2	+2.5	+1.8	+14.2	+1.6	+2.7
III	144.2	85.1/92	1.3	+2.2	−3.0	+13.1	+0.9	+3.7
IV	142.6	85.6/92	0.2	−0.1	+0.5	+2.7	−0.1	+0.3
V	144.1	83.2/92	1.3	−1.5	−5.7	−8.5	−1.4	−0.2
VI	143.3	83.9/92	0.8	−1.4	−5.4	−7.6	−1.4	−0.2
VII	143.6	84.4/92	1.0	−1.8	−5.1	−9.9	−1.7	−0.7
VIII	143.2	84.3/92	0.7	−1.1	−6.0	−11.1	−1.1	−0.5
X	145.2	85.5/92	1.9	+4.2	+1.8	+27.8	NA	NA
XI	144.3	83.5/92	1.4	−1.1	−3.3	−3.4	−1.1	+0.1
XII	143.2	84.2/92	0.7	−0.9	−3.3	−6.1	−0.9	−0.4

As shown in Table XII, once all Flatté parameters are allowed to float, none of the additional amplitudes has a significance above 3σ. This is different from the fixed-parameter Flatté tests in Sec. V A, where some additional amplitudes showed sizable apparent significances. The result indicates that the improvements previously attributed to additional amplitudes can largely be absorbed by changes in the $a_0(980)$ line shape.

To test whether a missing additional amplitude could mimic the observed shift of the $a_0(980)$ parameters, further fits are performed in which the complex coefficients of the additional amplitudes are fixed to the values obtained in Sec. V A, while the Flatté parameters are refitted. The resulting $\ln\mathcal{L}$ values, fit qualities, fitted $a_0(980)$ parameters, and pole positions are listed in Table XVI of Appendix B. Even with such artificially fixed additional components, the pole mass remains far above the near-threshold pole position calculated from the CLEO parameters.

Since the shift in M_{pole} is mainly driven by the fitted value of M_0, additional tests are performed by floating only M_0 while fixing the coupling constants to the CLEO values [14]. For each additional amplitude, three strategies are tested: fixing the full complex coefficient, fixing only its magnitude, or fixing only its phase to the value obtained in Sec. V A. The corresponding Flatté results are summarized in the Flatté columns of Tables XVIII, XIX, and XX in Appendix B, respectively.

In all these tests, the pole mass remains well above the near-threshold value calculated from the CLEO parameters. Moreover, for the same additional amplitude, the fitted M_{pole} can vary substantially depending on which part of the additional-amplitude coefficient is fixed. This instability indicates that these additional amplitudes do not provide a robust physical solution to the observed line shape discrepancy. In the fits listed in Table XX, where the phase of the additional amplitude is fixed and the magnitude is allowed to float, the fitted magnitudes for the models with amplitudes I, III, IV, and X are compatible with zero within statistical uncertainties. This further indicates that these components are not required by the data once the $a_0(980)$ line shape is allowed to vary.

These studies show that the Flatté parameterization can describe the data only by shifting the $a_0(980)$ pole mass well above the near-threshold region. Possible additional amplitudes, even when introduced with coefficients fixed from the fixed-parameter studies, cannot bring the pole mass back to the value calculated from the CLEO parameters. This demonstrates a tension between fit quality and the physical pole position in the direct-production Flatté description.

B. Floating the $a_0(980)$ parameters in the dispersively modified Flatté parameterization

As in the Flatté case, we first perform a fit in which only the coupling constants $g^2_{\pi\eta}$ and $g^2_{K\bar{K}}$ are floated, while M_0 is fixed to the value reported in Ref. [15]. The fit gives $\ln\mathcal{L} = 112.5$, $g^2_{\pi\eta} = (0.345 \pm 0.021)$ GeV$^2/c^4$, and $g^2_{K\bar{K}} = (0.341 \pm 0.057)$ GeV$^2/c^4$, with $\chi^2/\mathrm{NDOF} = 159.6/92$. The corresponding projections are shown in Fig. 12. The data are still not well described when only the two coupling constants are floated.

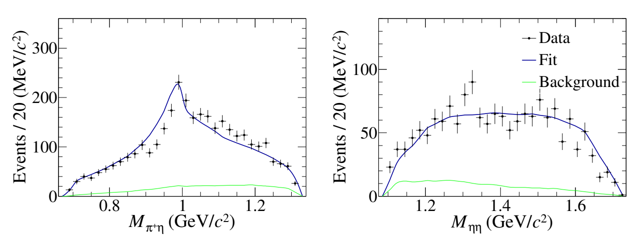

FIG. 12. The same as Fig. 3, but for the baseline fit by floating the $a_0(980)$ coupling constants with using dispersively modified Flatté parameterization for $P_{a_0(980)}$.

A further fit is performed by also floating M_0, while $g^2_{\pi\eta'}$ is fixed to the value reported in Ref. [15] due to the limited sensitivity to the $\pi\eta'$ channel. The fit returns $M_0 = (1.045 \pm 0.007_{\mathrm{stat}})$ GeV/c^2, $g^2_{\pi\eta} =$

$(0.319 \pm 0.026_{\rm stat})$ GeV$^2/c^4$, and $g^2_{K\bar{K}} = (0.416 \pm 0.064_{\rm stat})$ GeV$^2/c^4$. The fit gives $\ln\mathcal{L} = 144.6$ and χ^2/NDOF $= 84.5/92$. The projections are shown in Fig. 13. The corresponding pole position is $\sqrt{s}_{\rm pole} = [(1.087 \pm 0.009_{\rm stat}) - i(0.008^{+0.014}_{-0.008})]$ GeV$/c^2$. Both $M_{\rm pole}$ and $\Gamma_{\rm pole}/2$ differ significantly from the pole position calculated using the BESIII parameters reported in Ref. [15]. The pole mass is shifted well above the $K\bar{K}$ threshold, and $\Gamma_{\rm pole}/2$ becomes very small. Therefore, as in the Flatté case, although the data are well described after floating the $a_0(980)$ parameters, the resulting pole position is difficult to reconcile with the near-threshold nature of the $a_0(980)$.

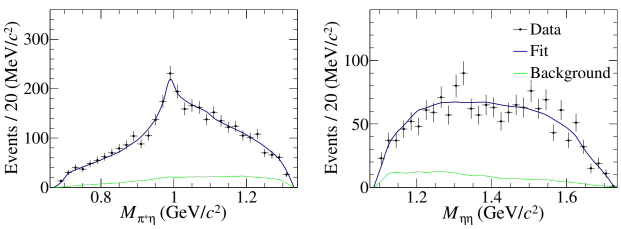

FIG. 13. The same as Fig. 3, but for the baseline fit by floating all $a_0(980)$ parameters with using dispersively modified Flatté parameterization for $P_{a_0(980)}$.

The systematic uncertainties of the floated $a_0(980)$ parameters and pole quantities are also evaluated. The considered sources and evaluation procedures are the same as those used in the Flatté case discussed in Sec. VI A. Only the IO check results and the effects from possible additional amplitudes are presented below, in Secs. VI B 1 and VI B 2, respectively. The resulting systematic uncertainties are summarized in Table XIII.

TABLE XIII. Systematic uncertainties for the $a_0(980)$ parameters and pole quantities obtained with the dispersively modified Flatté parameterization. The values are given in units of 10^{-2}; the units are GeV$/c^2$ for M_0, $M_{\rm pole}$, and $\Gamma_{\rm pole}/2$, and GeV$^2/c^4$ for the coupling constants. The fit-bias uncertainty, source IV, is not assigned for $\Gamma_{\rm pole}/2$ because, after retaining only poles on the $(-++)$ sheet in the IO check, its pull distribution cannot be described by a Gaussian function. The dash indicates that the corresponding uncertainty is not assigned and is not included in the total uncertainty.

Parameter	I	II	III	IV	V	VI	Total
M_0	0.3	0.1	0.2	0.0	0.0	0.4	0.5
$g^2_{\pi\eta}$	0.3	0.1	1.0	0.2	0.1	1.7	2.0
$g^2_{K\bar{K}}$	0.7	0.5	4.1	0.4	0.3	3.0	5.1
$M_{\rm pole}$	0.0	0.2	0.4	0.1	0.0	0.7	0.8
$\Gamma_{\rm pole}/2$	0.1	0.1	0.9	-	0.0	0.3	1.0

1. The IO Check

For $\Gamma_{\rm pole}/2$, the nominal value is very close to zero, suggesting that the pole is located close to the real axis and near the boundary between neighboring Riemann sheets. In the IO check, the pole associated with the $a_0(980)$ is found on a neighboring Riemann sheet in some pseudo-experiments. Following the pole-selection criterion used in the nominal analysis, only poles found on the $(-++)$ sheet are retained. For the retained pseudo-experiments, the pull distribution of $M_{\rm pole}$ can still be described by a Gaussian function, and the corresponding fit-bias uncertainty is evaluated. However, the pull distribution of $\Gamma_{\rm pole}/2$ cannot be described by a Gaussian function. Therefore, no fit-bias uncertainty is assigned for $\Gamma_{\rm pole}/2$. The IO check results for the remaining parameters are listed in Table XIV.

TABLE XIV. IO check results for the $a_0(980)$ parameters and pole mass obtained with the dispersively modified Flatté parameterization.

Parameter	μ_p	σ_p
M_0	0.02 ± 0.06	1.02 ± 0.04
$g^2_{\pi\eta}$	0.38 ± 0.06	1.03 ± 0.04
$g^2_{K\bar{K}}$	-0.29 ± 0.06	1.05 ± 0.04
$M_{\rm pole}$	0.18 ± 0.07	0.98 ± 0.05

Following the same correction procedure as that used in Sec. VI A 1, corrections are applied to $g^2_{\pi\eta}$, $g^2_{K\bar{K}}$, and $M_{\rm pole}$ according to the fitted pull means. The corrected results are $g^2_{\pi\eta,c} = (0.309 \pm 0.026_{\rm stat} \pm 0.020_{\rm syst})$ GeV$^2/c^4$, $g^2_{K\bar{K},c} = (0.435 \pm 0.064_{\rm stat} \pm 0.051_{\rm syst})$ GeV$^2/c^4$ and $M_{{\rm pole},c} = (1.085 \pm 0.009_{\rm stat} \pm 0.008_{\rm syst})$ GeV$/c^2$. Even after considering the systematic uncertainties, the corrected pole mass remains well above the pole mass calculated from the BESIII reference parameters.

2. Tests with additional amplitudes in the floating dispersive fit

The same additional amplitudes as those considered in Sec. V B are tested in the floating-parameter dispersively modified Flatté fit. The constant term is excluded from these tests, following the discussion in Sec. V B. For each additional amplitude, the fit is repeated with M_0, $g^2_{\pi\eta}$, and $g^2_{K\bar{K}}$ allowed to float, while $g^2_{\pi\eta'}$ is fixed to the value reported in Ref. [15]. The resulting $\ln\mathcal{L}$ values, fit qualities, significances of the additional amplitudes, and shifts in the fitted $a_0(980)$ parameters and pole quantities are summarized in Table XV. Here, "NA" indicates that no pole associated with the $a_0(980)$ is found on the $(-++)$ sheet; such fits are not used in the evaluation of the systematic uncertainty from additional amplitudes.

TABLE XV. Fit results obtained by adding one additional amplitude to the floating-parameter dispersively modified Flatté baseline model. The constant term is not included. All shifts are relative to the baseline fit with the dispersive parameters floated. The shifts are given in units of 10^{-2}, with GeV/c^2 for ΔM_0, $\Delta M_{\rm pole}$, and $\Delta(\Gamma_{\rm pole}/2)$, and GeV$^2/c^4$ for $\Delta g^2_{\pi\eta}$ and $\Delta g^2_{K\bar{K}}$. Here, "NA" indicates that no pole associated with the $a_0(980)$ is found on the $(-++)$ sheet.

Amplitude	$\ln\mathcal{L}$	χ^2/NDOF	Sig. (σ)	ΔM_0	$\Delta g^2_{\pi\eta}$	$\Delta g^2_{K\bar{K}}$	$\Delta M_{\rm pole}$	$\Delta(\Gamma_{\rm pole}/2)$
I	145.1	85.4/92	0.5	+0.5	−1.0	+3.0	NA	NA
II	147.0	84.1/92	1.6	+0.8	−1.1	+4.6	NA	NA
III	145.0	85.0/92	0.4	+0.4	−1.6	+2.4	NA	NA
IV	144.8	84.8/92	0.2	−0.1	−0.0	+1.0	−0.1	−0.3
V	145.7	83.0/92	1.0	−0.4	−1.7	−3.0	−0.7	+0.3
VI	144.9	83.6/92	0.3	−0.2	−1.3	−1.9	−0.4	+0.1
VII	144.9	84.4/92	0.3	−0.4	−0.9	−2.0	−0.5	+0.3
VIII	144.8	84.2/92	0.2	+0.1	−0.8	−1.5	−0.1	+0.0
X	145.7	85.8/92	1.0	−1.0	−1.9	+6.7	NA	NA
XI	145.2	84.1/92	0.6	−0.3	−0.9	−1.0	−0.4	+0.0
XII	144.8	84.0/92	0.2	−0.1	−0.4	−1.4	−0.2	+0.2

As shown in Table XV, once the dispersive parameters are allowed to float, none of the additional amplitudes has a significance above 3σ. This is different from the fixed-parameter dispersive tests in Sec. V B, where some additional amplitudes showed sizable apparent significances. The result indicates that the improvements previously attributed to additional amplitudes can largely be absorbed by changes in the $a_0(980)$ line shape.

To test whether a missing additional amplitude could mimic the observed shift of the $a_0(980)$ parameters, further fits are performed in which the complex coefficients of the additional amplitudes are fixed to the values obtained in Sec. V B, while the dispersive parameters are refitted. The resulting $\ln\mathcal{L}$ values, fit qualities, fitted $a_0(980)$ parameters, and pole positions are listed in Table XVII of Appendix B. Even with such artificially fixed additional components, the pole mass cannot be brought back to the near-threshold pole position calculated from the BESIII reference parameters.

As in Sec. VI A 2, additional tests are performed by floating only M_0 while fixing the coupling constants to the BESIII values [15]. For each additional amplitude, three strategies are tested: fixing the full complex coefficient, fixing only its magnitude, or fixing only its phase to the value obtained in Sec. V B. The corresponding dispersively modified Flatté results are summarized in the dispersive columns of Tables XVIII, XIX, and XX in Appendix B, respectively.

In all these tests, the pole mass remains well above the near-threshold value calculated from the BESIII reference parameters. This indicates that possible additional amplitudes, even when introduced with coefficients fixed from the fixed-parameter studies, cannot provide a robust solution to the observed pole-position shift.

These studies show that, as in the Flatté case, the dispersively modified Flatté parameterization can describe the data only by shifting the pole mass away from the near-threshold region. The additional-amplitude tests do not bring the pole mass back to the value calculated from the BESIII reference parameters, demonstrating the same tension between fit quality and the physical pole position.

VII. SUMMARY OF THE TESTS

The studies presented above show that the observed $a_0(980)$ line shape in $D^+ \to a_0(980)^+\eta$, $a_0(980)^+ \to \pi^+\eta$, cannot be satisfactorily described by the conventional direct-production amplitude models tested in this work. With the reference $a_0(980)$ parameters, the Flatté, dispersively modified Flatté, T-matrix, and K-matrix descriptions do not reproduce the data satisfactorily, even when additional conventional resonant or nonresonant amplitudes are included.

When the $a_0(980)$ parameters are allowed to float in the Flatté or dispersively modified Flatté parameterizations, the fit quality is significantly improved. However, the resulting pole mass is driven well above the $K\bar{K}$ threshold and cannot be brought back to the near-threshold region by systematic variations or by introducing additional amplitudes. Thus, the improved fit quality is obtained at the cost of a pole position that is difficult to reconcile with the usual near-threshold character of the $a_0(980)$.

These tests indicate that the distortion observed in the $a_0(980)$ line shape cannot be interpreted as evidence for a stable additional intermediate resonance within the conventional amplitude models considered here. Instead, the results point to a limitation of simple direct-production descriptions and suggest that mechanisms beyond the conventional tree-level amplitude picture may be relevant.

VIII. BRANCHING FRACTION MEASUREMENT

To measure the branching fraction of $D^+ \to \pi^+\eta\eta$, a selection optimized for the branching-fraction measurement is applied. The requirements $0.505 < M(\gamma\gamma)_\eta < 0.570$ GeV/c^2 and $\chi^2(\eta) < 50$ are imposed instead of the MVA selection used in the amplitude analysis.

The branching fraction is measured with the DT method [20]:

$$\mathcal{B}(D^+ \to \pi^+\eta\eta) = \frac{Y_{\rm DT}}{Y_{\rm ST}\,\epsilon_{\rm sig}\,\mathcal{B}^2_{\rm sub}}, \tag{38}$$

where $Y_{\rm DT}$ is the DT yield, $Y_{\rm ST}$ is the total single tag (ST) yield, $\epsilon_{\rm sig}$ is the weighted signal efficiency, and $\mathcal{B}_{\rm sub}$ denotes the branching fraction of $\eta \to \gamma\gamma$. The total ST yield is $Y_{\rm ST} = (10646.9 \pm 3.8) \times 10^3$. The weighted signal efficiency is defined as

$$\epsilon_{\rm sig} = \frac{\sum_i Y_{\rm ST}^{(i)}\,\epsilon_{\rm DT}^{(i)}/\epsilon_{\rm ST}^{(i)}}{Y_{\rm ST}}, \tag{39}$$

where $Y_{\rm ST}^{(i)}$, $\epsilon_{\rm ST}^{(i)}$, and $\epsilon_{\rm DT}^{(i)}$ are the ST yield, ST efficiency, and DT efficiency for the $i^{\rm th}$ tag mode, respectively.

The DT yield is extracted by fitting the ΔE distribution before applying the ΔE signal-window requirement, as shown in Fig. 14. The signal shape is described by the sum of a bifurcated Gaussian function and a double-Gaussian function. The bifurcated Gaussian function is a modified Gaussian function with different widths on the left and right sides of the peak. The two signal components share a common mean value. All signal-shape parameters except the common mean are fixed to the values obtained from the signal MC sample. The background shape is described by a second-order Chebyshev polynomial, which is validated with the inclusive MC sample. The fit gives $Y_{\rm DT} = 1506 \pm 49$.

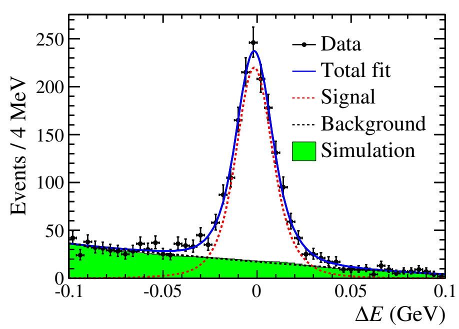

FIG. 14. Fit to the ΔE distribution. The black points with error bars represent data, the solid curve shows the total fit, the red dashed curve shows the signal component, and the black dashed curve shows the background component. The green histogram shows the background estimated from the inclusive MC sample.

The DT efficiency $\epsilon_{\rm DT}^{(i)}$ is determined with the signal MC sample. The signal MC sample is generated according to the amplitude model obtained from the fit to data using the Flatté parameterization with floated $a_0(980)$ parameters. This model reproduces the observed kinematic distributions and is used for the efficiency determination. The uncertainty associated with the generator model is evaluated by varying the model parameters according to the covariance matrix from the fit to data. The branching fraction is measured to be

$$\mathcal{B}(D^+ \to \pi^+\eta\eta) = (3.67 \pm 0.12_{\rm stat} \pm 0.06_{\rm syst}) \times 10^{-3}. \tag{40}$$

The systematic uncertainty is estimated to be 1.7%. The contributions are as follows. The uncertainties associated with PID, tracking, and η reconstructions are 0.5%, 0.5%, and 0.6%, respectively, and are determined from hadronic DT $D\bar{D}$ control samples [32]. The uncertainty from the signal shape is 0.6%, estimated by varying the fixed signal-shape parameters within their uncertainties and by replacing the nominal signal shape with the sum of a double-sided Crystal Ball function and a Gaussian function. The uncertainty from the background shape is 0.7%, estimated by fixing the polynomial parameters to those obtained from a fit to the simulated background sample from inclusive MC. The uncertainty associated with the $M_{\rm BC}$ signal window is found to be negligible. The uncertainty due to ST yield is 0.3%, taken from Ref. [32]. The uncertainty from the fit procedure is 0.3%, estimated with the inclusive MC sample using the same fitting procedure as applied to data. The MC-generator uncertainty is found to be negligible by varying the parameters in the generator model according to the covariance matrix obtained from the fit to data. The uncertainty from $\mathcal{B}(\eta \to \gamma\gamma)$ is 0.9% for two η mesons, taken from the PDG [6].

IX. CONCLUSION

Using 20.3 fb^{-1} of e^+e^- collision data collected with the BESIII detector at $\sqrt{s} = 3.773$ GeV, we perform the first amplitude analysis of the decay $D^+ \to \pi^+\eta\eta$. A prominent contribution from the decay chain $D^+ \to a_0(980)^+\eta$, $a_0(980)^+ \to \pi^+\eta$, is observed. No additional conventional resonant or non-resonant amplitude is found to provide a stable independent contribution to the signal model. The branching fraction of $D^+ \to \pi^+\eta\eta$ is measured to be $(3.67 \pm 0.12_{\rm stat} \pm 0.06_{\rm syst}) \times 10^{-3}$ using the DT method. Within the nominal amplitude model, in which only the $D^+ \to a_0(980)^+\eta$, $a_0(980)^+ \to \pi^+\eta$ decay chain is included, this value corresponds to the product branching fraction of the intermediate process.

The observed $\pi^+\eta$ mass spectrum exhibits an $a_0(980)$ line shape that differs from those observed in other processes. A systematic study is performed using several conventional descriptions of the $a_0(980)$ amplitude, including the Flatté parameterization, the dispersively modified Flatté parameterization, the T-matrix formalism, and the K-matrix formalism. With reference $a_0(980)$ parameters, these descriptions do not reproduce the observed line shape satisfactorily, even when additional conventional cascade decay amplitudes are included.

When the $a_0(980)$ parameters are allowed to float in the Flatté and dispersively modified Flatté parameterizations, the fit quality is significantly improved. However, the resulting pole mass is driven well above the $K\bar{K}$ threshold. This pole position is difficult to reconcile with the usual near-threshold character of the $a_0(980)$. Systematic variations and tests with additional amplitudes do not bring the pole mass back to the near-threshold region.

These results demonstrate a tension between the fit quality and the physical pole position in conventional direct-production amplitude models. The observed line shape distortion therefore cannot be explained solely by the choice of the $a_0(980)$ line shape parameterization or by interference with small additional conventional amplitudes. This suggests that additional dynamical effects beyond the conventional direct-production amplitude descriptions may be relevant for describing the $a_0(980)$ line shape in $D^+ \to \pi^+\eta\eta$.

The BESIII Collaboration thanks the staff of BEPCII (https://cstr.cn/31109.02.BEPC) and the IHEP computing center for their strong support. This work is supported in part by National Key R&D Program of China under Contracts Nos. 2023YFA1606000, 2023YFA1606704; National Natural Science Foundation of China (NSFC) under Contracts Nos. 12205384, 12175239, 12221005, 11635010, 11735014, 11935015, 11935016, 11935018, 12025502, 12035009, 12035013, 12061131003, 12192260, 12192261, 12192262, 12192263, 12192264, 12192265, 12221005, 12225509, 12235017, 12361141819; the Chinese Academy of Sciences (CAS) Large-Scale Scientific Facility Program; the CAS Center for Excellence in Particle Physics (CCEPP); Joint Large-Scale Scientific Facility Funds of the NSFC and CAS under Contract No. U1832207; CAS under Contract No. YSBR-101; 100 Talents Program of CAS; the Excellent Youth Foundation of Henan Scientific Commitee under Contract No. 242300421044; The Institute of Nuclear and Particle Physics (INPAC) and Shanghai Key Laboratory for Particle Physics and Cosmology; German Research Foundation DFG under Contract No. FOR5327; Istituto Nazionale di Fisica Nucleare, Italy; Knut and Alice Wallenberg Foundation under Contracts Nos. 2021.0174, 2021.0299; Ministry of Development of Turkey under Contract No. DPT2006K-120470; National Research Foundation of Korea under Contract No. NRF-2022R1A2C1092335; National Science and Technology fund of Mongolia; National Science Research and Innovation Fund (NSRF) via the Program Management Unit for Human Resources & Institutional Development, Research and Innovation of Thailand under Contract No. B50G670107; Polish National Science Centre under Contract No. 2019/35/O/ST2/02907; Swedish Research Council under Contract No. 2019.04595; The Swedish Foundation for International Cooperation in Research and Higher Education under Contract No. CH2018-7756; U. S. Department of Energy under Contract No. DE-FG02-05ER41374.

[1] M. Ablikim *et al.* [BESIII], Phys. Rev. Lett. **123**, 112001 (2019).
[2] M. Ablikim *et al.* [BESIII], Phys. Rev. D **104**, L071101 (2021).
[3] M. Ablikim *et al.* [BESIII], Phys. Rev. Lett. **132**, 131903 (2024).
[4] M. Ablikim *et al.* [BESIII], Phys. Rev. D **110**, L111102 (2024).
[5] M. Ablikim *et al.* [BESIII], Phys. Rev. Lett. **134**, 021901 (2025).
[6] S. Navas *et al.* [Particle Data Group], Phys. Rev. D **110**, 030001 (2024).
[7] M. Ablikim *et al.* [BESIII], Chin. Phys. C **37**, 123001 (2013).
[8] M. Ablikim *et al.* [BESIII], Phys. Lett. B **753**, 629-638 (2016) [erratum: Phys. Lett. B **812**, 135982 (2021)].
[9] M. Ablikim *et al.* [BESIII], Chin. Phys. C 48, 123001 (2024).
[10] S. M. Flatte, Phys. Lett. B **63**, 224-227 (1976)
[11] D. V. Bugg, Phys. Rev. D **78** (2008), 074023.
[12] N. Ikeno, M. Bayar and E. Oset, Eur. Phys. J. C **81**, 377 (2021).
[13] V. V. Anisovich, A. A. Kondashov, Y. D. Prokoshkin, S. A. Sadovsky and A. V. Sarantsev, Phys. Atom. Nucl. **63**, 1410-1427 (2000).
[14] G. S. Adams *et al.* [CLEO], Phys. Rev. D **84**, 112009 (2011).
[15] M. Ablikim *et al.* [BESIII], Phys. Rev. D **95**, 032002 (2017).
[16] J. Song, W. H. Liang and E. Oset, [arXiv:2502.20160 [hep-ph]].
[17] M. Albrecht *et al.* [Crystal Barrel], Eur. Phys. J. C **80**, 453 (2020)
[18] M. Ablikim *et al.* [BESIII], Nucl. Instrum. Methods Phys. Res., Sect. A **614**, 345 (2010).
[19] X. Wang *et al.*, JINST **11**, C08009 (2016).
[20] R. M. Baltrusaitis *et al.* [MARK-III], Phys. Rev. Lett. **56**, 2140 (1986).
[21] M. Ablikim *et al.* [BESIII], Phys. Rev. D **109**, 072003 (2024).
[22] S. Agostinelli *et al.* [GEANT4], Nucl. Instrum. Meth. A **506**, 250-303 (2003).
[23] D. J. Lange, Nucl. Instrum. Meth. A **462**, 152-155 (2001); R. G. Ping, Chin. Phys. C **32**, 599 (2008).
[24] J. C. Chen, G. S. Huang, X. R. Qi, D. H. Zhang and Y. S. Zhu, Phys. Rev. D **62**, 034003 (2000). R. L. Yang, R. G. Ping and H. Chen, Chin. Phys. Lett. **31**, 061301 (2014).
[25] A. Hocker *et al.*, *TMVA - Toolkit for Multivariate Data Analysis*, arXiv: physics/0703039; H. Voss, A. Hocker, J. Stelzer and F. Tegenfeldt, PoS **ACAT**, 040 (2007).
[26] B. S. Zou and D. V. Bugg, Eur. Phys. J. A **16**, 537-547 (2003).
[27] P. Rubin *et al.* [CLEO], Phys. Rev. D **78**, 072003 (2008).
[28] D. Evangelho Vieira, CERN-THESIS-2015-328.
[29] Z. H. Zhang and F. K. Guo, Phys. Lett. B **863**, 139387 (2025).
[30] B. Efron, "Bootstrap methods: Another look at the jackknife," *Ann. Statist.* **7**, 1–26 (1979).
[31] B. Efron and R. J. Tibshirani, *An Introduction to the Bootstrap*, Chapman & Hall/CRC, New York, 1993.

[32] M. Ablikim *et al.* [BESIII], Phys. Rev. Lett. **134**, 111801 (2025).

Appendix A: Projections for fits with additional amplitudes

This appendix presents the complete projection plots for the fits in which one additional conventional amplitude is added to the baseline model. The results are shown for the Flatté, dispersively modified Flatté, T-matrix, and K-matrix parameterizations of the $a_0(980)$ contribution. For each tested model, the left panel shows the $M(\pi^+\eta)$

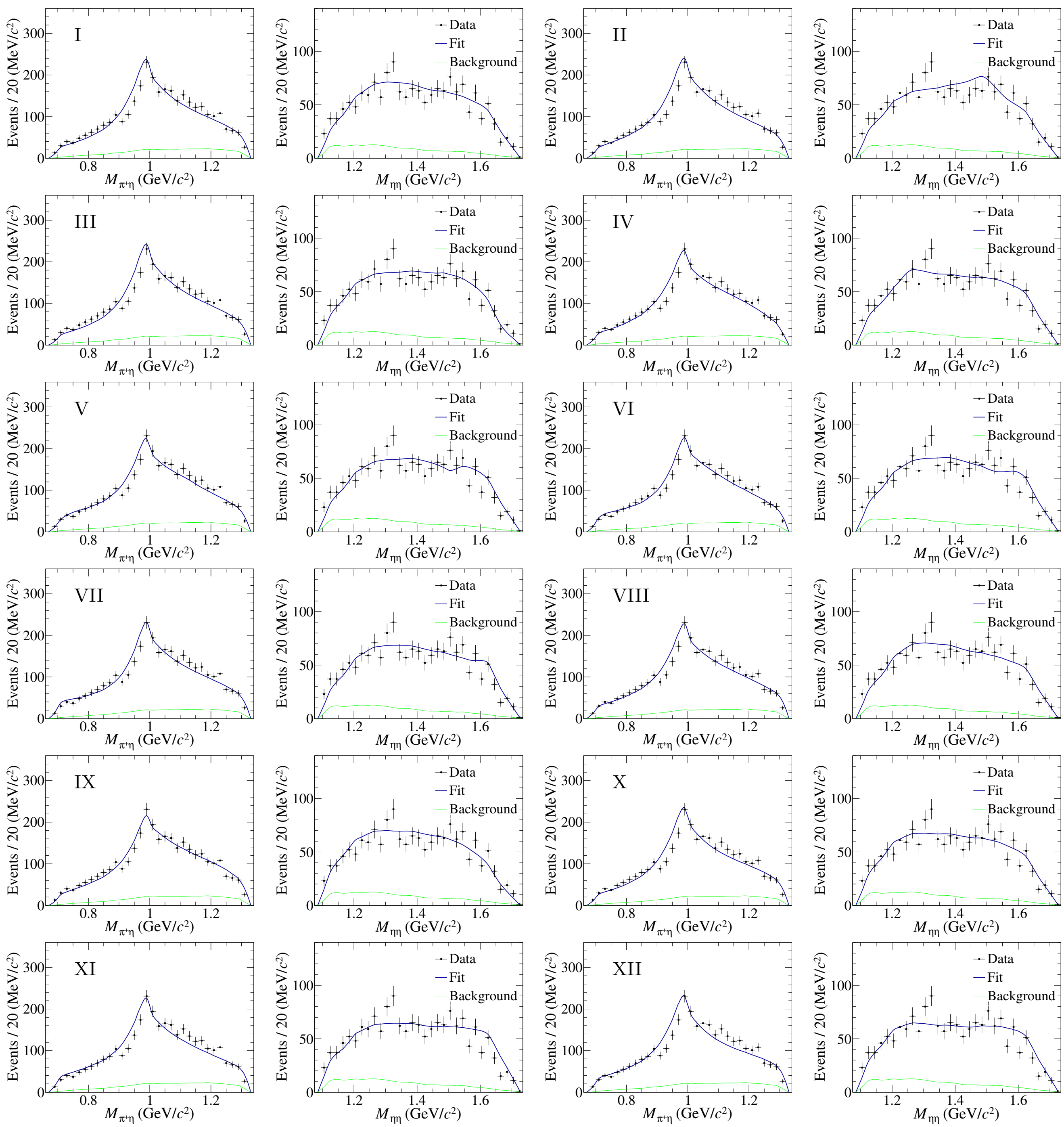

FIG. 15. The projections of (first and third columns) $M(\pi^+\eta)$ and (second and fourth columns) $M(\eta\eta)$ for model with further adding one amplitude using the Flatté parameterization for $P_{a_0(980)}$. The black dots with error bars are the data; the blue lines are the total fit; the green lines are the background. The amplitude numbers are the same as those listed in Table II.

projection and the right panel shows the $M(\eta\eta)$ projection. The model labels I–XII follow the definitions given in Table II.

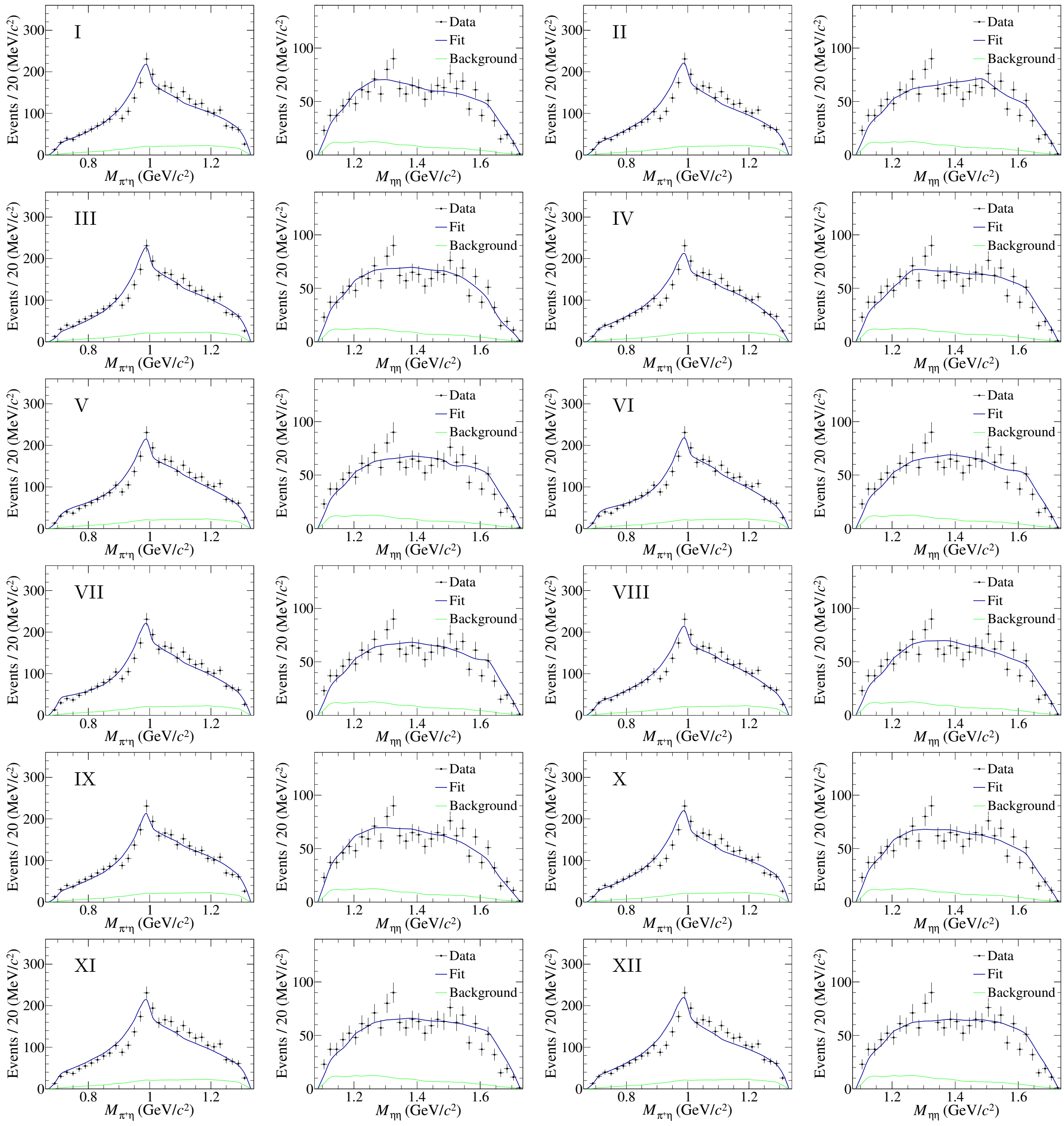

FIG. 16. The same as Fig. 15, but for the models using the dispersive parameterization for $P_{a_0(980)}$.

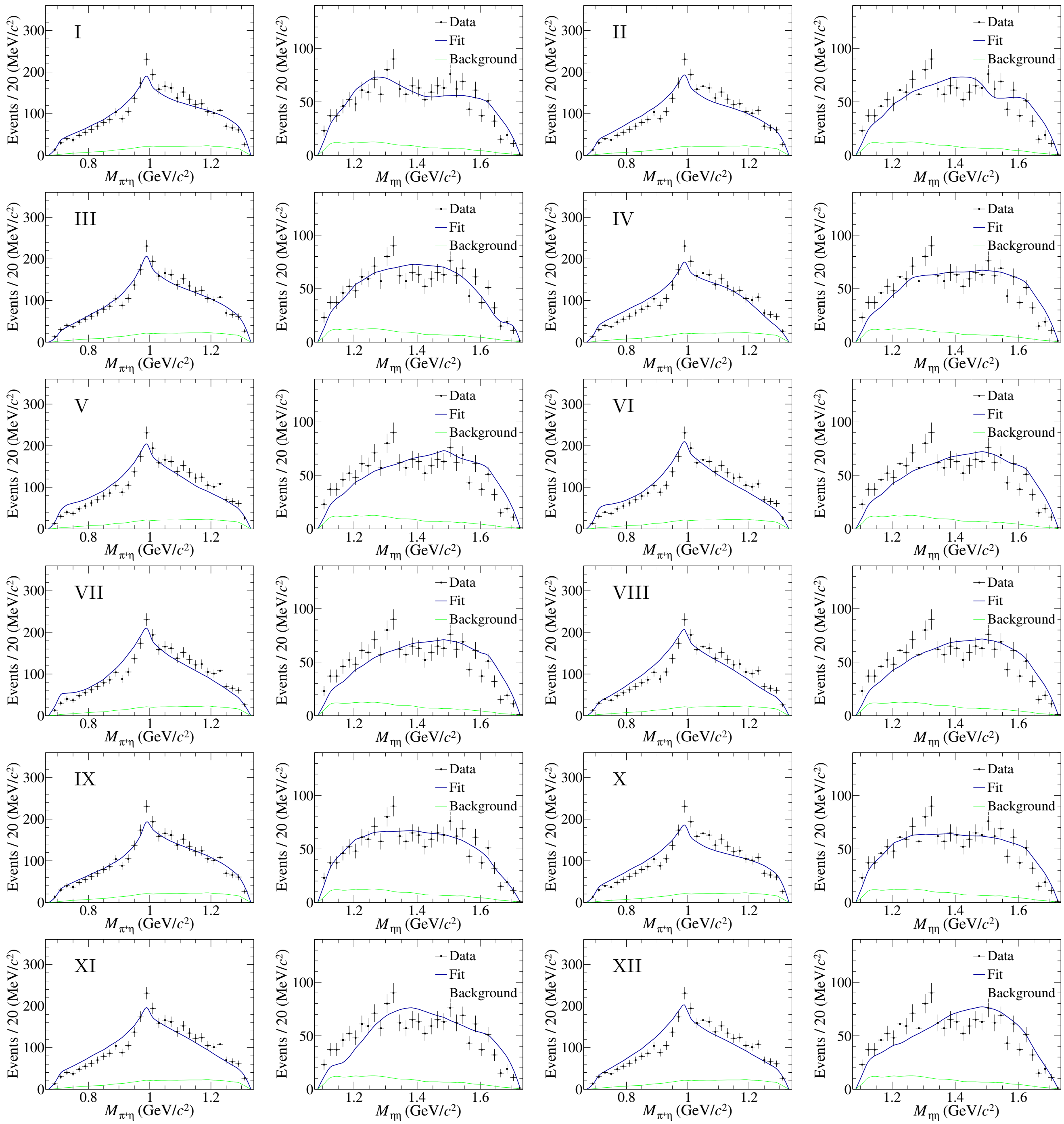

FIG. 17. The same as Fig. 15, but for the models using the T-matrix form instead of the $a_0(980)$ amplitude.

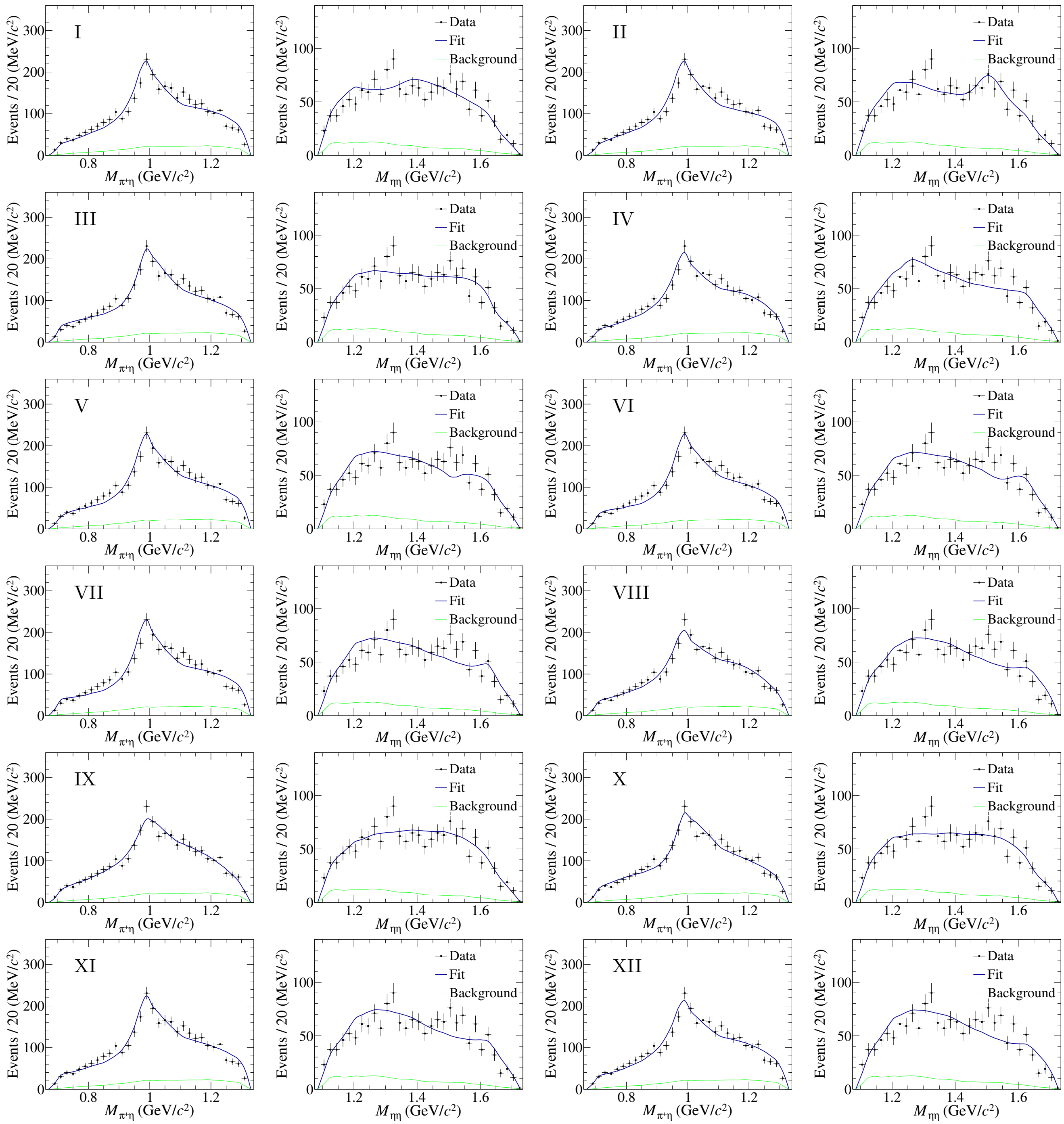

FIG. 18. The same as Fig. 15, but for the models using the K-matrix formula for the $a_0(980)$ line shape.

Appendix B: Additional tests with fixed additional-amplitude coefficients

This appendix gives the detailed results of additional tests in which the complex coefficients, magnitudes, or phases of possible additional amplitudes are fixed to the values obtained in the direct-production tests. These tests are performed to examine whether the shifted $a_0(980)$ pole position can be restored by including conventional additional amplitudes with fixed coefficients. The constant term is not included in these tests.

TABLE XVI. Fit results obtained by fixing the complex coefficient of each additional amplitude to the value obtained in Sec. V A, while refitting the Flatté parameters. The constant term is not included. The units are GeV/c^2 for M_0 and $\sqrt{s}_{\rm pole}$, and GeV$^2/c^4$ for $g^2_{\pi\eta}$ and $g^2_{K\bar{K}}$.

Amplitude	$\ln\mathcal{L}$	χ^2/NDOF	M_0	$g^2_{\pi\eta}$	$g^2_{K\bar{K}}$	$\sqrt{s}_{\rm pole}$
I	135.1	92.8/92	1.050 ± 0.009	0.421 ± 0.033	0.305 ± 0.081	$[(1.066 \pm 0.011) - i\,(0.081 \pm 0.017)]$
II	135.1	103.8/92	1.047 ± 0.009	0.398 ± 0.030	0.338 ± 0.081	$[(1.063 \pm 0.010) - i\,(0.069 \pm 0.016)]$
III	133.7	96.2/92	1.039 ± 0.008	0.445 ± 0.035	0.243 ± 0.072	$[(1.054 \pm 0.011) - i\,(0.101 \pm 0.016)]$
IV	135.1	96.3/92	1.052 ± 0.010	0.421 ± 0.034	0.474 ± 0.102	$[(1.070 \pm 0.010) - i\,(0.052 \pm 0.018)]$
V	136.4	98.0/92	1.039 ± 0.008	0.367 ± 0.024	0.337 ± 0.073	$[(1.055 \pm 0.008) - i\,(0.062 \pm 0.014)]$
VI	134.2	101.6/92	1.030 ± 0.007	0.370 ± 0.024	0.303 ± 0.067	$[(1.047 \pm 0.008) - i\,(0.069 \pm 0.013)]$
VII	136.9	99.5/92	1.032 ± 0.007	0.370 ± 0.023	0.265 ± 0.062	$[(1.048 \pm 0.008) - i\,(0.076 \pm 0.013)]$
VIII	137.2	89.0/92	1.043 ± 0.008	0.379 ± 0.025	0.298 ± 0.065	$[(1.059 \pm 0.009) - i\,(0.071 \pm 0.015)]$
X	136.7	88.4/92	1.056 ± 0.010	0.427 ± 0.034	0.358 ± 0.094	$[(1.073 \pm 0.012) - i\,(0.072 \pm 0.019)]$
XI	136.8	99.7/92	1.041 ± 0.007	0.359 ± 0.022	0.318 ± 0.062	$[(1.057 \pm 0.007) - i\,(0.062 \pm 0.013)]$
XII	141.2	87.5/92	1.057 ± 0.009	0.385 ± 0.026	0.375 ± 0.082	$[(1.073 \pm 0.010) - i\,(0.057 \pm 0.017)]$

TABLE XVII. Fit results obtained by fixing the complex coefficient of each additional amplitude to the value obtained in Sec. V B, while refitting the dispersive parameters. The constant term is not included. The units are GeV/c^2 for M_0 and $\sqrt{s_{\rm pole}}$, and GeV$^2/c^4$ for $g^2_{\pi\eta}$ and $g^2_{K\bar{K}}$. Here, "NA" indicates that no pole associated with the $a_0(980)$ is found on the $(-++)$ sheet.

Amplitude	$\ln\mathcal{L}$	χ^2/NDOF	M_0	$g^2_{\pi\eta}$	$g^2_{K\bar{K}}$	$\sqrt{s}_{\rm pole}$
I	137.9	89.5/92	1.032 ± 0.006	0.346 ± 0.025	0.322 ± 0.059	$[(1.078 \pm 0.009) - i\,(0.042 \pm 0.018)]$
II	141.5	92.1/92	1.035 ± 0.006	0.318 ± 0.024	0.367 ± 0.058	$[(1.077 \pm 0.009) - i\,(0.024 \pm 0.015)]$
III	136.7	95.2/92	1.021 ± 0.006	0.374 ± 0.025	0.267 ± 0.056	$[(1.069 \pm 0.009) - i\,(0.067 \pm 0.016)]$
IV	139.7	94.9/92	1.034 ± 0.007	0.324 ± 0.025	0.490 ± 0.073	NA
V	139.4	96.6/92	1.032 ± 0.006	0.313 ± 0.023	0.406 ± 0.059	$[(1.072 \pm 0.008) - i\,(0.016 \pm 0.014)]$
VI	135.8	104.0/92	1.024 ± 0.006	0.333 ± 0.023	0.383 ± 0.057	$[(1.068 \pm 0.008) - i\,(0.031 \pm 0.015)]$
VII	137.3	103.6/92	1.025 ± 0.006	0.343 ± 0.023	0.339 ± 0.054	$[(1.071 \pm 0.008) - i\,(0.042 \pm 0.016)]$
VIII	140.0	88.4/92	1.032 ± 0.006	0.334 ± 0.025	0.387 ± 0.054	$[(1.077 \pm 0.009) - i\,(0.025 \pm 0.015)]$
X	138.7	88.9/92	1.031 ± 0.006	0.344 ± 0.025	0.296 ± 0.055	$[(1.076 \pm 0.008) - i\,(0.047 \pm 0.017)]$
XI	143.3	89.7/92	1.037 ± 0.006	0.300 ± 0.022	0.397 ± 0.052	$[(1.076 \pm 0.008) - i\,(0.012^{+0.016}_{-0.007})]$
XII	144.7	84.0/92	1.044 ± 0.007	0.318 ± 0.025	0.408 ± 0.063	$[(1.086 \pm 0.009) - i\,(0.010^{+0.019}_{-0.006})]$

TABLE XVIII. Fit results obtained by floating only M_0 while fixing the coupling constants to the reference values and fixing the full complex coefficient of each additional amplitude to the value obtained in Secs. V A and V B. For the Flatté parameterization, the coupling constants are fixed to the CLEO values; for the dispersively modified Flatté parameterization, they are fixed to the BESIII values. The constant term is not included. The units are GeV/c^2 for M_0 and M_{pole}.

Amplitude	Flatté				Dispersively modified Flatté			
	$\ln\mathcal{L}$	χ^2/NDOF	M_0	M_{pole}	$\ln\mathcal{L}$	χ^2/NDOF	M_0	M_{pole}
I	132.9	95.6/92	1.047 ± 0.007	1.062 ± 0.006	137.2	92.5/92	1.033 ± 0.006	1.084 ± 0.007
II	134.2	104.8/92	1.043 ± 0.007	1.058 ± 0.006	139.5	98.2/92	1.037 ± 0.006	1.088 ± 0.006
III	128.7	102.7/92	1.036 ± 0.007	1.053 ± 0.006	135.8	97.8/92	1.022 ± 0.006	1.073 ± 0.006
IV	132.0	101.1/92	1.042 ± 0.007	1.057 ± 0.006	136.9	101.4/92	1.030 ± 0.006	1.081 ± 0.007
V	136.3	98.1/92	1.037 ± 0.007	1.054 ± 0.006	136.8	104.3/92	1.031 ± 0.006	1.082 ± 0.006
VI	134.1	101.5/92	1.030 ± 0.007	1.048 ± 0.006	134.7	108.7/92	1.023 ± 0.006	1.074 ± 0.006
VII	136.5	99.8/92	1.033 ± 0.007	1.050 ± 0.006	136.5	107.7/92	1.026 ± 0.006	1.076 ± 0.006
VIII	136.8	89.2/92	1.043 ± 0.007	1.058 ± 0.006	139.1	91.4/92	1.031 ± 0.006	1.082 ± 0.007
X	134.2	91.7/92	1.050 ± 0.008	1.064 ± 0.006	137.2	94.2/92	1.032 ± 0.006	1.084 ± 0.006
XI	136.8	99.7/92	1.041 ± 0.007	1.056 ± 0.006	139.0	101.9/92	1.037 ± 0.006	1.089 ± 0.006
XII	140.4	87.7/92	1.053 ± 0.007	1.067 ± 0.006	142.9	89.2/92	1.044 ± 0.007	1.096 ± 0.007

TABLE XIX. Fit results obtained by floating only M_0 while fixing the coupling constants to the reference values and fixing only the magnitude of each additional amplitude to the value obtained in Secs. V A and V B. For the Flatté parameterization, the coupling constants are fixed to the CLEO values; for the dispersively modified Flatté parameterization, they are fixed to the BESIII values. The constant term is not included. The units are GeV/c^2 for M_0 and M_{pole}.

Amplitude	Flatté				Dispersively modified Flatté			
	$\ln\mathcal{L}$	χ^2/NDOF	M_0	M_{pole}	$\ln\mathcal{L}$	χ^2/NDOF	M_0	M_{pole}
I	137.1	99.0/92	1.059 ± 0.009	1.072 ± 0.008	137.9	101.9/92	1.040 ± 0.011	1.091 ± 0.011
II	136.9	100.9/92	1.055 ± 0.010	1.068 ± 0.009	143.9	91.5/92	1.050 ± 0.008	1.102 ± 0.008
III	138.3	92.7/92	1.063 ± 0.010	1.076 ± 0.009	136.4	93.6/92	1.026 ± 0.008	1.077 ± 0.008
IV	135.1	88.5/92	1.053 ± 0.010	1.067 ± 0.009	137.1	100.8/92	1.030 ± 0.006	1.081 ± 0.007
V	138.0	93.6/92	1.044 ± 0.010	1.060 ± 0.009	136.8	104.4/92	1.031 ± 0.006	1.082 ± 0.006
VI	134.4	100.9/92	1.031 ± 0.007	1.048 ± 0.006	134.9	107.7/92	1.024 ± 0.006	1.075 ± 0.007
VII	136.7	100.0/92	1.033 ± 0.007	1.050 ± 0.006	137.2	104.8/92	1.028 ± 0.007	1.079 ± 0.007
VIII	136.9	89.2/92	1.043 ± 0.007	1.058 ± 0.006	139.2	91.0/92	1.032 ± 0.007	1.083 ± 0.007
X	136.7	92.1/92	1.059 ± 0.009	1.072 ± 0.008	142.4	93.3/92	1.047 ± 0.008	1.098 ± 0.009
XI	138.1	96.4/92	1.045 ± 0.008	1.061 ± 0.007	140.5	97.1/92	1.042 ± 0.007	1.093 ± 0.007
XII	140.5	86.6/92	1.053 ± 0.008	1.067 ± 0.006	142.9	89.0/92	1.044 ± 0.007	1.096 ± 0.007

TABLE XX. Fit results obtained by floating only M_0 while fixing the coupling constants to the reference values and fixing only the phase of each additional amplitude to the value obtained in Secs. V A and V B. For the Flatté parameterization, the coupling constants are fixed to the CLEO values; for the dispersively modified Flatté parameterization, they are fixed to the BESIII values. The constant term is not included. The units are GeV/c^2 for M_0 and M_{pole}.

Amplitude	Flatté				Dispersively modified Flatté			
	$\ln\mathcal{L}$	χ^2/NDOF	M_0	M_{pole}	$\ln\mathcal{L}$	χ^2/NDOF	M_0	M_{pole}
I	136.8	92.3/92	1.056 ± 0.008	1.070 ± 0.007	142.8	89.8/92	1.044 ± 0.007	1.096 ± 0.008
II	137.3	93.5/92	1.052 ± 0.009	1.066 ± 0.007	142.9	89.2/92	1.045 ± 0.008	1.097 ± 0.008
III	137.0	92.0/92	1.059 ± 0.010	1.072 ± 0.009	143.0	88.4/92	1.041 ± 0.008	1.093 ± 0.009
IV	136.8	92.1/92	1.056 ± 0.010	1.069 ± 0.008	142.9	89.8/92	1.043 ± 0.007	1.094 ± 0.008
V	139.4	91.3/92	1.047 ± 0.008	1.061 ± 0.007	142.8	89.7/92	1.044 ± 0.008	1.096 ± 0.008
VI	138.3	91.9/92	1.045 ± 0.009	1.060 ± 0.008	142.8	89.6/92	1.044 ± 0.008	1.096 ± 0.008
VII	137.7	92.5/92	1.049 ± 0.009	1.063 ± 0.008	143.1	90.5/92	1.041 ± 0.008	1.093 ± 0.008
VIII	139.2	87.5/92	1.049 ± 0.008	1.063 ± 0.007	142.8	89.4/92	1.043 ± 0.009	1.094 ± 0.009
X	136.9	93.0/92	1.057 ± 0.009	1.070 ± 0.007	142.9	90.2/92	1.046 ± 0.008	1.097 ± 0.008
XI	141.0	88.5/92	1.050 ± 0.008	1.064 ± 0.007	142.8	89.9/92	1.044 ± 0.007	1.096 ± 0.007
XII	140.6	86.8/92	1.053 ± 0.008	1.067 ± 0.007	142.9	89.3/92	1.044 ± 0.007	1.096 ± 0.007